

Microstructural Constraints on Magmatic Mushes under Kīlauea Volcano, Hawai'i

Penny E. Wieser^{*1}, Marie Edmonds¹, John Maclennan¹ and John Wheeler²

¹ Department of Earth Sciences, University of Cambridge, Downing Street, Cambridge, UK, CB2 3EQ.

² Department of Earth, Ocean and Ecological Sciences, University of Liverpool.

* Corresponding author: pew26@cam.ac.uk

Abstract

Distorted olivines of enigmatic origin are ubiquitous in erupted products from a wide range of volcanic systems (e.g., Hawai'i, Iceland, Andes). Investigation of these features at Kīlauea Volcano, Hawai'i, using an integrative crystallographic and chemical approach places quantitative constraints on mush pile thicknesses. Electron back-scatter diffraction (EBSD) reveals that the microstructural features of distorted olivines, whose chemical composition is distinct from undistorted olivines, are remarkably similar to olivines within deformed mantle peridotites, but inconsistent with an origin from dendritic growth. This, alongside the spatial distribution of distorted grains and the absence of adcumulate textures, suggests that olivines were deformed within melt-rich mush piles accumulating within the summit reservoir. Quantitative analysis of subgrain geometry reveals that olivines experienced differential stresses of 3-12 MPa, consistent with their storage in mush piles with thicknesses of a few hundred metres. Overall, our microstructural analysis of erupted crystals provides novel insights into mush-rich magmatic systems.

Introduction

Studies of the textural and geochemical characteristics of olivine crystals have revealed significant complexity in basaltic volcanic plumbing systems, including the timescales of eruptive triggering from diffusion profiles¹, storage times from crystal chemistry², and depths of magma storage from melt inclusion geochemistry³. Olivines with prominent lattice distortions are commonplace in olivine-rich basalts from a range of tectonic settings^{2,4,5}. As the magmatic processes producing distorted olivines are poorly understood, these features represent a previously unexploited source of information.

At Kīlauea Volcano, distorted olivines are commonly attributed to ductile creep within dunitic bodies located around the central conduit⁶ or within the deep rift zones (~5–9 km depth)^{7,8}. However, a recent suggestion that lattice distortions are produced by an early phase of

branching dendritic growth, followed by textural ripening and the merging of misoriented crystal buds, has gained considerable traction^{5,9}. Lattice distortions have also been attributed to collisions between crystals during magma flow through constricted or irregular conduits^{10,11}.

Establishing the magmatic processes producing distorted olivines is vital to further our understanding of basaltic plumbing systems. Extracting the information held within these features is particularly crucial at Kīlauea, where olivine is the only silicate phase in magmas containing >6.8 wt% MgO^[12] so provides the main record of pre-eruptive storage. Furthermore, Kīlauean primary melts have ~15–17 wt% MgO¹³, yet erupted lavas contain 5–10 wt% MgO, and few crystals (1–3 vol%)¹⁴. This disparity in MgO contents requires fractionation and storage of considerable volumes of olivine within the volcanic edifice¹⁵.

Materials with high seismic velocities (interpreted as dunitic bodies) have been imaged within the summit region and deep rift zones of Kīlauea Volcano¹⁶. Large earthquakes, slow slip events, and landslides have been attributed to the presence of these weak dunitic bodies separating the south flank of Kīlauea from the rest of the island of Hawai'i^{15,17}. Yet, the relationship between distorted olivines in erupted products and seismically-imaged dunites remains unresolved. If lattice distortions are created within dunitic bodies, microstructural interrogation may provide insights into the instability of the south flank. However, if distortions are in fact growth features, the association between dunitic bodies and edifice instability at ocean islands (e.g., Hawai'i, Reunion) may have been overestimated from petrological observations of distorted grains⁵. The hypothesis that distorted olivines originate from dunitic bodies has fuelled suggestions that Kīlauea's deep rift zones allow magma to bypass the summit reservoir⁸. Re-assessing the petrological evidence for summit bypass is vital for accurate estimates of magma supply rates and CO₂ fluxes at Kīlauea¹⁸.

If distorted olivines record plastic deformation, rather than crystal growth processes, their microstructures can be evaluated within the conceptual framework developed through the extensive study of naturally- and experimentally-deformed mantle peridotites. The movement of dislocations is one of the main mechanisms accommodating plastic deformation within crystals. Dislocations can be characterized in terms of a Burgers vector (\vec{b}) and a line direction (\vec{u}). The plane containing these vectors defines the slip plane¹⁹. The angle between \vec{b} and \vec{u} determines whether the dislocation is an edge dislocation ($\vec{b} \perp \vec{u}$), a screw dislocation ($\vec{b} \parallel \vec{u}$), or a mixed dislocation (\vec{b} and \vec{u} neither parallel or perpendicular). A slip system is described in terms of a set of slip planes, and a Burgers vector direction on which dislocation motion occurs. For example, the olivine slip system (010)[100] denotes the movement of edge

dislocations along the (010) plane with a [100] Burgers vector direction. Previous work has identified five olivine fabric types (A to E-types) from different crystallographically preferred orientations (CPOs), and determined the role that pressure, temperature, differential stress and hydration exert on their formation^{20–22}. However, unlike thin sections of mantle peridotites, the orientations of erupted olivines in tephra and spatter deposits have been randomised upon eruption and again during sample preparation, so CPOs cannot be used to infer deformation conditions in volcanic olivines. Fortunately, CPOs are macroscopic features resulting from the activities of different dislocation types, which can be classified in terms of slip systems^{21,23–26}.

Until now, most assessments of lattice distortion in volcanic olivines have used optical microscopy^{6,8,27}. This method is largely qualitative, and optical evidence for distortion is often ambiguous in small grains, or across subgrain boundaries with small misorientations (see **Supplementary Figs. 1-5**)²⁸. A few studies have employed more quantitative methods at Kīlauea, but these have been restricted to visual examination of dislocation structures and densities following oxidation decoration of dislocations^{29,30}, and examination of lattice strain using in situ X-ray diffraction²⁸. In this study, low angle boundaries in individual olivine crystals within basaltic spatter and scoria from Kīlauean eruptions were mapped using electron backscatter diffraction (EBSD). This method not only offers significant improvements in spatial and angular resolution compared to optical observations (**Supplementary Figs. 1-5**)³¹, it also provides sufficient crystallographic information to quantify the Burgers vector and slip plane, and thus the dominant slip system (see **Methods**). As many deformation experiments on mantle-derived olivines were conducted at pressures and temperatures similar to those found within igneous plumbing systems (e.g., 250–300 MPa, 1200°C)³², assessment of the activities of different slip systems in erupted olivine crystals places constraints on the conditions of deformation (using established links between slip systems, CPOs and fabric types, and between fabric types and deformation conditions)^{21,23–26}. Finally, to evaluate the suggestion that lattice distortion results from the textural maturation of olivine dendrites, we assess the crystallographic signatures of branching dendritic growth in olivine dendrites from West Greenland picrites^{33,34}, and compare these to microstructures in distorted Kīlauean olivines.

We demonstrate that distorted olivines show microstructures which are remarkably similar to those observed in naturally- and experimentally-deformed mantle peridotites, but distinct from the crystallographic signatures of dendritic growth. These findings, alongside the spatial distribution of distorted olivines, indicate that lattice distortions formed during high temperature creep in melt-rich olivine mush piles at the base of the summit reservoir.

Results and Discussion

Incidence of lattice distortions

We examine olivines from a wide range of eruptions temporally associated with activity at Mauna Ulu (May 1969 - December 1974). This five year period is distinct in Kīlauea's history; eruptions occurred almost simultaneously on the East and South West rift zones (ERZ; SWRZ), and at discrete sites within and around the summit caldera (Fig. 1)³⁵. Thus, this suite of eruptions provides a unique opportunity to decipher the spatial distribution of distorted olivines within a single eruptive period at Kīlauea (see **Supplementary Table 1** for sample details). We also investigate two further SWRZ eruptions; the circumferential lava flow on the seismic SWRZ (~1700 AD)³⁶ and the Mauna Iki eruption on the volcanic SWRZ (1919–1920 AD)³⁷.

Up to now, distorted olivines were thought to be reasonably rare in subaerial eruptions compared to submarine eruptions at Kīlauea^{6,15,38}. Yet, we find abundant distorted grains in subaerially erupted products from all ERZ eruptions (Pauahi crater, Episode 1 and 12 of Mauna Ulu) and seismic SWRZ eruptions (1974; ~1700 AD; Fig. 1). Spatter from Mauna Iki on the volcanic SWRZ also contains a significant number of distorted grains. In contrast, erupted products from four intra-caldera summit eruptions and the 1971 volcanic SWRZ eruption contain very few distorted grains. In almost all eruption products, distorted grains are more abundant in sieved fractions >1 mm²⁹; Fig. 1). The 1971 Volcanic SWRZ spatter contain very few grains >1 mm (4 in ~150 g), but all are distorted, whereas no grains <1 mm show distortion. Intracaldera summit eruptions (August, 1971, September 1971, July 1974, September 1974) contain no grains >1 mm, but all distorted grains are >840 μm.

Evaluating the Dendritic Growth Hypothesis

First, we test the hypothesis that lattice distortions are produced during an early phase of branching dendritic growth, followed by textural re-equilibration during periods of reduced undercooling⁵. Due to a change in olivine-melt partitioning during rapid dendritic growth, high concentrations of phosphorous (P) are incorporated into the crystal structure³⁹. While the external morphology of dendritic crystals evolves during subsequent textural re-equilibration to obscure this early growth phase, slow diffusion rates preserve internal P enrichments⁴⁰. The presence of P-rich zones passing across extinction discontinuities would be one of the main lines of evidence supporting the dendritic growth hypothesis^{5,9}. However, wavelength-dispersive spectroscopy (WDS) maps collected by electron microprobe reveal homogenous cores within almost all distorted grains (Fig. 2). Similar findings have been reported for olivines

from Kīlauea Iki²⁷. One P-rich zone terminates against a subgrain boundary (Fig. 2d), suggesting that P enrichments and subgrains did not form during the common process of dendritic growth. Instead, the rapid growth episode generating the P zoning may have preceded the distortion of the crystal lattice, perhaps separated by a dissolution episode (c.f., ref. ⁵). Thus, while some olivines at Kīlauea may have experienced an early dendritic growth phase, this process appears unrelated to the production of lattice distortions.

Furthermore, if distorted olivines represent texturally-matured dendrites, the crystallographic signatures of dendritic growth and lattice distortion should be identical. We examine low-angle subgrain boundaries in 137 distorted olivine crystals from Kīlauea, and compare them to the crystallographic signature of dendritic branching in 61 olivine dendrites from West Greenland³³. Most branching dendritic buds in the West Greenland olivines show identical crystallographic orientations to the primary crystal; merging of such buds cannot produce lattice distortions. The 125 misorientated crystal buds (Fig. 3a) show a bimodal distribution of misorientation axes, with a strong maximum around [010]⁴¹ and a weaker maximum around [100] (Fig. 3c)^{34,41}. Misorientation angles are predominantly <20°, but extend up to 90.5° (Fig. 3d)³⁴. In contrast, lattice distortions in Kīlauean olivines show misorientation axes predominantly between [010] and [100] (Fig. 4c), and small (<5°) misorientation angles. The boundary between dendritic buds and the host crystal display [010] and [001] WBVDs (Fig. 3b), while lattice distortions show predominantly [100] WBVDs, with some [001] vectors (Fig. 4b). Finally, the interior of dendritic olivines display no low-angle boundaries with [100] or [001] Burgers vectors.

These crystallographic differences imply that lattice distortions are not produced by textural maturation of olivine dendrites. Instead, the misorientation axes and WBVDs in distorted olivines are indicative of slip systems similar to those invoked to cause CPOs in olivine deformation experiments at conditions resembling Kīlauea's plumbing system⁴². Crucially, in contrast to olivine dendrites, Kīlauean olivines exhibit very few [010] WBVDs (consistent with experimental observations that slip on [010] is unusual due to the long length of the b lattice vector⁴³). Thus, we propose that lattice distortions represent true deformation of the crystal lattice, rather than growth features.

Collisions of Crystals

The indistinguishable major element chemistry of deformed and undeformed grains^{6,38}, along with euhedral grain outlines, has led to suggestions that deformation results from grain collisions during magma flow through constricted conduits^{10,11}. However, deformed grains examined in this study have higher forsterite contents than undeformed grains (Fig. 5a-b), with statistically significant differences for individual eruptions ($p < 0.01$, Kolmogorov-Smirnov test,

Fig. 5c-f). Differences in minor element compositions have also been reported for deformed and undeformed grains erupted at Kīlauea Iki²⁷. Finally, deformed olivines in different eruptions have similar forsterite contents, which are significantly out of equilibrium with their matrix glasses. In contrast, undeformed olivines show more chemical variability, and many plot closer to the equilibrium composition (Fig. 5a-b). These observations cannot be reconciled with late stage crystal-crystal collisions, which would result in deformed and undeformed grains having indistinguishable chemistry²⁷, and the same degree of disequilibrium with co-erupted matrix glasses.

Generating Differential Stresses within Volcanic Plumbing Systems

The majority of deformed olivines at the Earth's surface are derived from mantle peridotites. However, deformed Kīlauean olivines are unlikely to be mantle xenocrysts for two principal reasons. Firstly, almost all deformed Kīlauean olivines have high CaO contents (>0.2 wt%), while the deformed olivines in mantle peridotites and plutonic rocks typically have <0.1 wt% CaO^{15,44} (Fig. 6a). Secondly, many deformed Kīlauean olivines have inclusions of melt and euhedral spinels, indicating growth within the volcanic system^{8,29}. These observations suggest that these olivines grew, and were subsequently deformed within Kīlauea's plumbing system.

To generate lattice distortions, crystals must be subject to non-hydrostatic stress⁶. Previously, olivine deformation has been attributed to differential stresses exerted within Kīlauea's deep rift zone dunites, during the downward flow of olivine from the summit area to the rift zones, or rapid rift zone extension during south flank earthquakes¹⁵. However, mechanisms involving deep rift zone processes require specific magma transport paths to bring deformed crystals to the surface. For example, the presence of deformed grains in lavas from the Mauna Ulu eruption have led to suggestions that magma is transported along the basal decollement⁸. However, significant magma transport through the deep rift zones is at odds with geophysical observations, which demonstrate no measurable changes in rift zone opening rates during magma supply surges or rift zone eruptions¹⁸ and generally supports shallow (< 2 km) magma transport⁴⁵. Given the wide spatial and temporal distribution of deformed grains identified in this study, it seems untenable that every eruption received a significant contribution to its olivine crystal cargo from deep rift zone transport paths.

The textural features of deformed olivines are also inconsistent with an origin from low melt fraction dunites (<5 % melt)¹⁵. Olivines derived from such bodies would be expected to show adcumulate textures similar to those found in xenoliths erupted at Kīlauea Iki⁶ and post-shield Hawaiian lavas⁴⁶. Instead, most distorted grains have subhedral-euhedral outlines with no internal melt films and high angle grain boundaries (Fig. 4). While corrosion followed by

overgrowth can produce euhedral crystals from disaggregated dunites⁴⁷, this process would preserve internal melt films.

A crucial observation is the fact that deformed olivines have been noted in a variety of basaltic systems. Vinet et al.⁴ report their presence in all five of the volcanic centres which they examined in the Andean Southern Volcanic Zone. Deformed olivines have also been noted in the Vaigat formation of West Greenland³³, the Baffin Bay volcanic province⁴⁸, Piton de la Fournaise volcano⁵, and the Loch Uisg area, Mull⁴⁹. This implies that olivines are deformed by a process which is near-ubiquitous in a wide range of volcanic plumbing systems. We suggest that a plausible mechanism is gravitational loading within melt-rich cumulate piles with ~40% porosity⁵⁰ produced by crystal settling². Such an origin accounts for the global distribution of deformed grains, and the absence of adcumulate textures at Kīlauea. To investigate this hypothesis further, we assess the location, and conditions under which deformation occurred.

Assessing the conditions of deformation

Dominant slip systems in low-angle subgrain boundaries were assessed by calculating misorientation axes, Weighted Burgers Vector directions (WBVDs), and boundary wall geometries from EBSD maps. This approach resolves the ambiguities involved when using misorientation axes alone to determine slip systems⁵¹. For example, tilt walls consisting of (100)[001] or (001)[100] edge dislocations (described in terms of (slip plane)[Burgers Vector]) and twist walls consisting of (010)[100] and (010)[001] screw dislocations all produce misorientation axes about [010]. However, WBVDs (which can be highlighted by color coding of EBSD maps; e.g., Fig 4b) can distinguish between these three boundary types: (100)[001] tilt walls would show [001] WBVDs (red), (001)[100] tilt walls would show [100] WBVDs (green), and twist walls would show mixes of [100] and [001] WBVDs (green via yellow to red). The geometry of the subgrain boundary provides further discriminatory power. Tilt walls contain the misorientation axis within the boundary plane, while twist wall boundary planes are perpendicular to the misorientation axis (Fig. 7a-b). For simplicity, it was assumed that subgrain boundaries showed pure tilt or twist character. Detailed descriptions of the code and classification criteria used to identify slip systems is provided in the **Methods**.

Approximately 83% and 17% of boundaries were classified as tilt and twist walls respectively. These observations are consistent with literature observations that olivine subgrain walls with [100] WBVDs tend to have edge character⁴³, and the fact that the majority of WBVDs are [100] or [001] (Fig. 4,7c), rather than mixed directions (e.g., a WBVD parallel to [101] would appear yellow). Conditions of deformation were deduced from the slip system proportions in the more prevalent tilt walls. Boundaries related to (010)[100], {0kl}[100] and (001)[100] slip comprised

~30%, ~44% and ~16% of the total length of tilt boundaries respectively (Fig. 8a). These findings imply that [100] slip systems represent the primary slip systems, with the mosaicity of crystallographic orientation in some olivine grains (Fig. 4) resulting from secondary (100)[001] and (010)[001] slip (~6% and ~3% of boundaries respectively; Fig. 8a).

Experimental work shows that (010)[100] slip, producing A-type fabrics in deformed mantle peridotites, dominates in hot, dry, low stress environments²². Slip on (001)[100], producing E-type fabrics, occurs at similar pressure, temperature and stress conditions to A-type fabrics, but is favoured by a higher water content (Fig. 8c)²¹. The strengths of these two slip systems are comparable at pressures of 300 MPa, and olivine water contents of ~200 H/10⁶Si_{molar}²¹. The conditions producing D-type fabrics are debated, they may involve high stresses, low temperatures and low water contents favouring slip on {0kl}[100]^{20,23}. Alternatively, crystallographic signatures indicative of {0kl}[100] slip may be produced when (010)[100] and (001)[100] edge dislocations are present within a single subgrain boundary³⁶. Overall, the dominance of slip systems with [100] WBVDs in Kīlauean olivines is indicative of deformation at moderate-high temperatures and low-moderate water contents (Fig. 8a). To further constrain the deformation conditions, and assess the origin of {0kl}[100] slip, we place independent constraints on differential stresses and olivine water contents.

Differential stresses were estimated using subgrain and dislocation density piezometry. As both methods apply to steady state microstructures, they likely represent minimum stress estimates. Subgrain piezometry utilizes the empirical relationship between subgrain-size (d) and differential stress (σ)⁵²:

$$\sigma = \frac{45\mu b}{d} \quad (1)$$

where μ is the shear modulus (65x10⁹ Pa), b is the magnitude of the Burgers vector (5x10⁻¹⁰ m) and d is the distance between subgrain boundaries in m.

Subgrain sizes were assessed using an adapted linear intercept method suitable for EBSD maps of individual olivines. The distances between boundaries with [100] WBVDs and misorientations >0.5° were measured perpendicular to the mean boundary trace (**Supplementary Fig. 6**), rather than along predefined directions in specimen coordinates (c.f. ref⁵³). Distances were converted into estimates of differential stress using equation 1. Subgrain differential stress estimates show a prominent peak at ~3–12 MPa, with 95% of the stresses lying between ~3 and 30 Mpa (Fig. 8b).

Dislocation-density piezometry utilizes the relationship between dislocation densities (ρ) and differential stress (σ)⁴²:

$$\sigma = \sqrt{\frac{s \rho b^2}{B}} * \mu \quad (2)$$

Where $B=1.74 \times 10^{-3}$ and $s=1.37$.

Sakyi et al.²⁹ report dislocation densities measured using the oxidative decoration technique in a variety of picritic basalts from Kīlauea and Mauna Loa (including some from Mauna Ulu). While they do not report dislocation densities for specific eruptions, their textural descriptions of “blocky olivines” are very similar to our observations of distorted grains. Blocky olivines have dislocation densities of $1\text{--}5 \times 10^{10} \text{ m}^{-2}$, yielding differential stress estimates of $\sim 4\text{--}11$ MPa. Despite estimates pertaining to different samples, and the large uncertainties associated with each method, stress estimates from subgrain piezometry and dislocation densities are in close agreement (Fig. 8b). Olivine water contents of $H/10^6 \text{Si}_{\text{molar}}=20\text{--}280$ were calculated from H_2O measurements in olivine-hosted melt inclusions from multiple Kīlauean eruptions⁵⁴ and olivine-melt partition coefficients ($K_D = 0.0013\text{--}0.0021$ ⁵⁵; orange bar; Fig. 8c).

The low differential stresses estimated from linear intercept distances and dislocation densities are difficult to reconcile with the conventional interpretation that misorientation axes lying between [001] and [010] represent slip on the relatively high stress {0kl}[100] system. Instead, our data support the hypothesis that a {0kl}[100]-like misorientation axis distribution is generated by the presence of (010)[100] and (001)[100] edge dislocations within a single subgrain boundary³⁶. Slip on (010)[100] dominates at low-moderate stresses and low-moderate water contents, while (001)[100] slip dominates is favoured by higher water contents⁵⁶ (Fig. 8c). Our independent estimates of olivine water contents and differential stresses lie at this transition where the strengths of (010)[100] and (001)[100] slip are comparable²¹. Thus, it is highly probable that subgrain walls in Kīlauean olivines apparently relating to {0kl}[100] slip are actually made from mixtures of (010)[100] and (001)[100] type dislocations. This reconciles our independent estimates of deformation conditions from subgrain piezometry and the microstructural analysis of slip system proportions.

Mush pile geometry

The distribution of differential stress estimates from subgrain and dislocation density piezometry (predominantly $\sim 3\text{--}12$ MPa) allows assessment of the hypothesis that volcanic

olivines are deformed by gravitational loading within melt-rich mush piles. Differential stresses (σ_D) in mush piles scale as a function of the density difference between crystals and host melts ($\Delta\rho$), and the thickness (H):

$$H = \frac{\sigma_D}{g \cdot \Delta\rho} \quad (3)$$

Where $g=9.8 \text{ m/s}^2$, and $\Delta\rho=567 \text{ kg/m}^3$ (using $\rho=3282 \text{ kg/m}^3$ for Fo_{86} olivine at 1230°C ⁵⁷, and $\rho=2715 \text{ kg/m}^3$ for the interstitial basaltic liquid^{54,58}).

Using this simple equation, the measured differential stresses may be generated at the bottom of mush piles ~540–2160 m thick. However, centuries of observations have demonstrated that a near-ubiquitous feature of granular materials is the arrangement of solid particles into force chains, resulting in unequal transmission of load (e.g. corn in silos, stacked fruit, poppy seeds; photoelastic particles)^{59–62}. Highly stressed chains of primary members transmit most of the force, while a larger group of secondary members experience less than the mean force, and a few spectator particles experience no force (Fig. 9b)⁶³. The settling of dense olivine crystals into mush piles creates a crystal framework with ~40% porosity⁵⁰, which constitutes a granular medium. Thus, it is highly probable that mush piles contain force chains. Simulations of mush piles show that the proportion of particles experiencing more than the mean force has an exponential distribution, with forces on certain grains exceeding 6x the mean force⁶⁰. Dynamical phenomena within magma chambers (e.g., magma injection) drive the migration of force chains, resulting in a large proportion of olivines experiencing greater than the mean force⁶⁰. This process could reduce the required mush pile thickness by a third, to ~180–720 m.

More precise constraints on mush pile thicknesses in igneous systems from investigations of deformed volcanic crystals will require several conceptual advances. Numerical simulations of granular mush piles are computationally expensive, despite only considering spherical particles in 2D⁶⁰. In reality, the force applied at contacts between angular crystals will be amplified into very high stresses by small contact areas⁶⁴. Such highly heterogeneous stress distributions within individual grains^{64,65} complicate piezometric estimates. An increased understanding of how heterogeneous stresses within individual grains are translated into subgrain sizes and dislocation densities is needed, alongside discrete-element models accounting for force chain geometry in three dimensions, using realistic crystal shapes. Finally, transitions between a predominantly frictional regime (with force chains) to a lubricating regime may occur within mush piles, affecting the amount of stress amplification⁶⁰. An alternative research direction would be to perform EBSD on olivines at the base of mush piles of known

thickness in extinct volcanic systems (where intrusions outcrop at the surface), to produce a calibration between deformation intensity and mush pile thickness.

Mush pile location

The spatial distribution of deformed grains across the Kīlauean edifice provides insights into the location of mush piles. Geophysical and geochemical observations at Kīlauea have led to a model in which magma is stored at two distinct depths^{66–68}. We find the largest proportion of deformed olivines in eruptions derived from the deeper South Caldera (SC) reservoir (based on Pb isotopes)^{67,68}. In contrast, there are few deformed grains in intracaldera and volcanic SWRZ eruptions which tap the upper, more evolved Halema'uma'u reservoir. The different sources of these eruptions is also evident from the higher Mg# of co-erupted glasses in eruptions containing abundant deformed grains (Fig. 5a-b), consistent with the storage of more primitive melts in the deeper SC reservoir^{67,69}. Interestingly, unlike the 1971 SWRZ eruption, the 1919–1920 Mauna Iki eruption contains abundant deformed grains (both eruptions occurred on the volcanic SWRZ). This supports the hypothesis that the Mauna Iki eruption tapped magma from multiple reservoirs based on the decoupling of E-W and N-S tilt components³⁷.

Crucially, the commonality between eruptions containing deformed grains is that a significant proportion of their magma supply (and thus crystal cargo) was derived from the SC reservoir. An origin for deformed grains within mush piles at the base of this reservoir is a simpler explanation for their abundance in a wide variety of subaerial eruptions than invoking magma transport paths along the basal decollement⁸. The narrow range of forsterite contents in deformed grains in our study ($\sim\text{Fo}_{87}$; Fig. 5) may result from diffusive re-equilibration of Mg and Fe during prolonged mush pile storage^{2,70}. The scavenging of deformed grains from mush piles just before eruption also explains the high degree of olivine-liquid disequilibrium between deformed grains and their host melts⁷⁰. As the Halema'uma'u reservoir is thought to be recharged from the SC reservoir⁶⁷, entrainment of a small number of deformed grains during recharge events can account for their occasional occurrence in intracaldera eruptions, and the more extreme difference in forsterite contents between deformed and undeformed grains in these eruptions (Fig. 5e).

To further assess the hypothesis that deformed grains form in mush piles accumulating at the base of the SC reservoir, we explore the timescales required to generate the mush pile thicknesses indicated by subgrain piezometry ($\sim 180\text{--}720$ m) using a simple box model informed by available geophysical and geochemical constraints at Kīlauea. Primary melts with 16.5 wt% MgO enter a cylindrical sill at a rate of $0.1\text{ km}^3/\text{yr}$ ⁷¹ (Fig. 10a). Within the sill, olivine

crystals form and settle into cumulate piles (~40% porosity), causing the remaining liquid to evolve to lower MgO contents. This liquid leaves the reservoir, and is either erupted, or stored within the deep rift zones⁷¹. Fractionation from primary liquids to the average whole rock MgO contents of erupted lavas (~10 wt% MgO) requires removal of ~14 volume % olivine cumulate¹⁵. The thickness of the cumulate pile in the sill is a play off between reservoir radius and accumulation time (Fig. 10b). Geodetic observations of surface displacements by interferometric synthetic aperture radar (InSAR) can be modelled as a magma chamber represented by penny-shaped cracks with radii of ~2–4 km^[72]. This geometry permits accumulation of ~180–720 m of mush with ~40% porosity in just a few centuries (Fig. 10). This is consistent with the diverse range of trace element ratios within melt inclusions in any given eruption, which indicate minimum mush pile residence times of >170 yrs⁷⁰. Thus, our hypothesis that deformed grains are generated by gravitational loading within mush piles accumulating within the SC reservoir is supported by available geometric and temporal constraints. Under this framework, deformed olivines are not archives of processes occurring within Kīlauea's deep rift zones. However, the absence of petrological evidence for dunitic bodies does not imply their absence (c.f. ref⁵). Many deep processes within igneous systems are not manifested in erupted products⁷³, but still play a crucial role in the evolution of volcanic systems.

The temporal evolution of mush piles at the base of the deeper SC reservoir is uncertain. To resolve space problems, olivine must eventually migrate downslope to form the seismically imaged dunitic bodies¹⁵ (Fig. 9a). We suggest that the amount of interstitial melt gradually reduces during this process, leading to the generation of true adcumulate textures, with internal melt films and high angle grain boundaries. Additional stress imposed during downslope flow accounts for the higher differential stresses estimated from subgrain piezometry in dunitic xenoliths from Hualalai (40±20 MPa vs. 3-12 MPa)⁴⁶. Deformed olivines from the ~1700 AD eruption may record the first stages of this process; they contain prominent low and high angle boundaries (misorientations <10° and >10° respectively; Fig 6b-c). The latter are decorated with thin films of melt (Fig. 6b), indicating derivation from low melt fraction bodies. These olivines also show trails of secondary fluid inclusions, similar to those observed in Hawaiian xenoliths¹⁵. Finally, these olivines have substantially lower forsterite contents than other deformed olivines (~Fo_{82–83} vs. ~Fo_{86–88}; Fig. 5a-b), and several have Ca contents overlapping with values measured in Hualalai dunites⁴⁶ (Fig. 6a). These chemical differences may reflect cooling during transport away from the main magma storage region at Kīlauea. Texturally similar olivines have also been identified in the Kīlauea Iki eruption⁶. Eruptions sampling these more consolidated dunitic bodies are clearly uncommon, and may be restricted to those ascending along infrequently utilized pathways to the surface⁶.

Microstructural analysis constraints mush processes

A quantitative examination of microstructures in distorted olivines erupted at Kīlauea Volcano by electron backscatter diffraction reveals striking similarities to deformed mantle peridotites, but significant differences to the crystallographic signatures of dendritic growth. This suggests that lattice distortions record the application of differential stresses at high temperatures within the magmatic plumbing system, rather than rapid crystal growth. Previous petrological work has concluded that differential stresses are applied during the creep of dunitic bodies within Kīlauea's rift zones. Crucially, this has fuelled suggestions that significant quantities of magma bypass the summit reservoir and travel along the deep rift zones, despite the paucity of geophysical evidence for this process. In contrast, we suggest that olivine crystals are deformed in gravitationally-loaded olivine mush piles at the base of the deeper South Caldera reservoir, explaining the spatial distribution of grains at Kīlauea, and the absence of adcumulate textures. Moreover, the mechanism we propose here accounts for the occurrence of deformed grains in a wide variety of basaltic systems worldwide, which lack deep rift zones.

Application of piezometers developed for mantle peridotites reveals that deformed olivines experienced differential stresses of ~3–12 MPa. Assuming that olivine mush piles behave as granular materials, and form force chains, the vertical extent of mush piles at Kīlauea can be estimated (~180-720 m). Based on available constraints on the magma supply rate, and the geometry of Kīlauea's summit reservoir, these thicknesses accumulate in a few centuries.

Overall, microstructural investigations of erupted olivine crystals by EBSD generates rich datasets which provide quantitative insights into crystal storage within mush piles. Under the increasingly prevalent view that crustal magmatic systems are mush-dominated⁷⁴, constraining the geometry and dynamics of crystal storage regions is crucial to further our understanding of magmatic plumbing systems. The presence of deformed olivines in many different volcanic settings highlights the global applicability of the methods developed in this study. Furthermore, assessments of deformation conditions using EBSD need not be restricted to olivine-bearing samples. Microstructural fabrics types in natural and experimental samples have been established for a wide variety of igneous phases (e.g. diopside⁷⁵, plagioclase⁷⁶, hornblende⁷⁷), extending the applicability of our study to more evolved igneous systems.

Methods

Sample preparation

The vesicular nature of the basaltic scoria from Kīlauea Volcano is not amenable to thin section production. Additionally, due to the high modal proportion of vesicles, few olivines are

found within each thin section. Instead, tephra and lava samples were jaw crushed and sieved into three size fractions (> 1 mm, 840–250 µm and <250 µm). Olivine crystals were picked and mounted in epoxy stubs based on their crystal size (allowing stubs to be variably ground down such that the cores of crystals were exposed). A sample of West Greenland picrite, and one Kīlauean epoxy grain mount were made into thin sections to allow comparisons between optical and EBSD observations (**Supplementary Figs. 1-5**). Epoxy mounts and thin sections were polished with progressively finer silicon pastes, then colloidal silica using a VibroMet 2 Buehler Vibratory Polisher.

EBSD analysis

EBSD data was collected on a FEI Quanta 650FEG SEM equipped with a Bruker e-Flash HR EBSD detector in the Department of Earth Sciences, University of Cambridge. Data collection and indexing was performed with Bruker QUANTAX CrystaAlign. The step size of each acquisition was varied depending on the size of the aggregate such that each map took ~15-20 mins to collect (see **Supplementary Table 2** for additional acquisition parameters). EBSD data clean up and post-processing was performed in MTEX V5.0.4⁷⁸, an open-source toolset for MATLAB. Single misindexed pixels were removed, and data was denoised using a 5 neighbour Kuwahara filter³¹.

EPMA analysis

Electron microprobe spot analyses and wavelength-dispersive spectroscopy (WDS) maps of olivine were performed using a Cameca SX100 EPMA in the Department of Earth Sciences, University of Cambridge. Olivine spot analyses were conducted in several analytical sessions, with slight variations in analytical conditions. Count times and calibration materials, alongside estimates of precision and accuracy are shown in **Supplementary Table 3**. Precision and accuracy were calculated from repeated measurements on a San Carlos Olivine secondary standard. Within each run, deformed and undeformed grains from each eruption were analysed in roughly equal proportions. Thus, chemical differences between deformed and undeformed grains cannot be attributed to analytical variation.

Matrix glasses from 10 eruptions were analysed in a single analytical session at 15kV, 6nA, using a 5 µm defocused beam (samples KL0908, KL0909, KL0910, KL0914, KL0916, KL0917, KL0919, KL0920, KL0922, KL0931). Glass compositions for samples KL0921,

KL0930 and KL0924 were taken from Sides et al. (ref. ⁵⁴; codes 1700g, 1920g and 1974J2 respectively). Count times and calibration materials, alongside estimates of precision and accuracy are shown in **Supplementary Table 4** and **5**. Precision and accuracy were calculated from repeated measurements on VG2 and Basalt_113716-1.

WDS maps of phosphorus and other elements were collected at 15 kV, 200 nA, with a spot size of 1 μm (see **Supplementary Table 6** for details). The pixel size was varied between 3-6 μm depending on the size of the olivine, with a dwell time of 400 ms. The total acquisition time for each map varied between 3-17 hrs.

Slip System Identification

The classification of a grain as distorted or undistorted is somewhat arbitrary, particularly based on optical observations^{28,29}. Here, the presence of distortion was quantitatively assessed by identifying subgrain boundaries using the calcGrains MTEX function, with a threshold angle of 0.5°. Olivines were classified as distorted if at least 1 low angle boundary stretching across ~ a third of the crystal was identified. The use of smaller threshold angles than 0.5° would result in imprecise estimates of misorientation axes and angles, due to the finite angular resolution of conventional EBSD^{79,80}. Furthermore, utilization of smaller threshold angles can result in inaccurate stress estimates from microstructural methods such as subgrain piezometry⁵³.

The same detector resolution was used for all EBSD acquisitions, and pixel spacings were significantly smaller than the microstructure features of interest (3–10 μm vs. ~100 μm), resulting in a consistent definition of a distorted crystal. The shape of the boundary and relation to external morphological features in BSE images were visually assessed to ensure that grains containing low angle boundaries resulting from grain aggregation³⁴ were not considered further (e.g., the boundaries between euhedral grains in Fig. 2d).

To allow comparison of our EBSD data with previous studies utilizing optical microscopy at Kīlauea, EBSD maps for ~20 grains within a ~40 μm thick section were compared to optical observations. Low angle boundaries with misorientations <1° are extremely difficult to see optically, even with a high-spec optical microscope (Zeiss Axioscope A1; **Supplementary Figs. 1-5**). Additionally, the ability to optically resolve subgrain boundaries depended on the sharpness of the misorientation contrast, and the orientation of the crystal within the thin section. In some instances, subgrain boundaries with misorientations up to 2.5° were invisible. Based on the small subset of grains examined here, previous optical studies may have

underestimated the proportion of distorted grains by up to 45%. This is similar to the conclusions of Sakyi et al.²⁹ who observe dislocation textures in optically undeformed grains.

We quantify the dislocations present (and thus the dominant slip systems) within distorted olivine crystals using two metrics that can be obtained from EBSD data; the misorientation across a boundary, and the Weighted Burgers Vector Direction (WBVD). The misorientation describes the axis-angle pair of the coordinate transform from the crystallographic orientation on one side of the boundary to that across the boundary. Misorientations are stated in terms of a misorientation axis and the minimum angle of rotation about this axis⁸¹. For example, a misorientation of 3° about [010] shows that the crystallographic directions of two adjacent subgrains can be superimposed by a rotation of 3° about the olivine b axis.

The Weighted Burgers Vector direction (WBVD) quantifies the weighted mean of the Burgers vectors of all types of geometrically necessary dislocation in a local region, assessed using 2D orientation gradients in EBSD maps (see ref⁸² for more detail). This is also expressed in terms of a crystallographic direction (e.g. [100]). The WBVD depends on the dislocation density for each type, and is weighted towards dislocation lines at a high angle to the map. For discrete boundaries, the apparent dislocation density and hence the WBV magnitude depends on pixel spacing, but the WBV direction (WBVD) does not, and provides sufficient crystallographic information to assess slip system occurrence. Specifically, the WBVD samples the Burgers vectors of dislocations in low-angle boundaries and cannot introduce any illusory directions which are not present in the actual microstructure.

Crucially, EBSD allow assessment of the misorientation and WBVDs for lots of neighbouring pixels along a given low angle boundary, and large numbers of individual low angle boundaries in relatively short acquisition times (15-20 mins per grain), and processing times (~2 minutes per grain). The large datasets generated using these methods are crucial for the precise characterisation of microstructures in volcanic olivines which show only subtle distortions.

Subgrain boundaries within individual EBSD maps were classified using new code built in MTEX 5.0.4^[78], incorporating WBVD calculations from CrystalScape⁸². Firstly, misorientation axes were calculated for boundary segments with misorientation angles between 0.5–10°. Boundaries were classified as twist walls if they met the following criteria: a) angle between the misorientation axis and the z direction in specimen coordinates >15° and b) angle between the misorientation axis and the grain boundary trace in specimen coordinates >75°. Criteria a) accounts for the fact that boundaries with low dips are unlikely to be observed⁸². Crucially, this rules out misidentification of a tilt boundary orientated such that the misorientation axis is near

vertical as a twist wall. The second criteria accounts for the theoretical geometry of a twist wall (Fig. 7b), where the misorientation axis is perpendicular to the boundary trace (allowing for 15° leniency). Boundaries were classified as tilt walls if: c) the boundary was not classified as a twist wall and d) the normal to the plane containing the grain boundary trace and misorientation axis (i.e., the normal to the tilt boundary plane) in specimen coordinates was >15° from the z direction (discarding boundaries with low dips). For example, boundary pixels within the pink rectangle (Fig. 7c) meet criteria b) but not a), as the misorientation axes are nearly vertical (blue dots; Fig. 7d). Thus, boundary pixels were classified as a tilt walls, as they met condition c) and condition d). This tilt wall is orientated with a near vertical boundary plane and misorientation axis.

As this method classified only ~17% of boundaries as twist walls, slip system proportions were quantitatively assessed in the more prevalent (and more geometrically simple) tilt walls. Within a single grain, tilt boundaries with a given WBVD displayed a narrow range of boundary traces (Fig. 7c), allowing isolation of tilt boundaries with [100] and [001] WBVD. For boundaries displaying each WBVD, the direction of the misorientation axis for each boundary segment was compared to the misorientation axis (in crystal coordinates) expected for each slip system (Fig. 7e). Slip system proportions were calculated in two ways; by summing the total length of each boundary type, and by calculating the proportion of each boundary type in a single grain, and averaging these values (N=62 grains, Fig. 8a).

Linear Intercept Method

Linear intercepts are traditionally measured along predetermined directions (e.g. horizontal and vertical) within entire thin sections. We adapt this method for use on EBSD maps of individual deformed olivine crystals. Instead of measuring along arbitrary directions, we measure distances perpendicular to low angle boundaries with [100] WBVDs within the interior of the crystal. Distances between the outermost subgrain boundary and the edges of the crystal were not used, as this distance depends on the amount of crystal preserved during jaw crushing, and the extent of crystal growth following entrainment into erupting magmas (see **Supplementary Fig. 6**). It was decided that sectioning effects were negligible compared to the uncertainty stemming from different parameterizations of the relationship between subgrain size and differential stresses⁵³.

Data Availability

All compositional data obtained in this study are included as supplementary data tables.

Code Availability

The Matlab scripts used to classify olivine slip systems (run in MTEX 5.0.4) have been uploaded into the supplementary information with an example .ctf file of the distorted grain shown in the middle row of Fig. 4.

References

1. Rae, A. S. P. *et al.* Time scales of magma transport and mixing at Kīlauea Volcano, Hawai'i. *Geology* **44**, 463–466 (2016).
2. Thomson, A. & MacLennan, J. The Distribution of Olivine Compositions in Icelandic Basalts and Picrites. *Journal of Petrology* **54**, 745–768 (2013).
3. Tuohy, R. M., Wallace, P. J., Loewen, M. W., Swanson, D. A. & Kent, A. J. R. Magma transport and olivine crystallization depths in Kīlauea's east rift zone inferred from experimentally rehomogenized melt inclusions. *Geochimica et Cosmochimica Acta* **185**, 232–250 (2016).
4. Vinet, N., Molina, P. & Flemming, R. Quantification and origin of intracrystalline deformation of olivine from basalts of the Andean Southern Volcanic Zone: A multidisciplinary study. *Congreso Geologica Chileno* (2015).
5. Welsch, B., Faure, F., Famin, V., Baronnet, A. & Bachèlery, P. Dendritic Crystallization: A Single Process for all the Textures of Olivine in Basalts? *Journal of Petrology* **54**, 539–574 (2013).
6. Helz, R. Diverse olivine types in lava of the 1959 eruption of Kilauea volcano and their bearing on eruption dynamics. *Volcanism In Hawaii 1* 691–722 (1987).
7. Clague, D. A., Moore, J. G., Dixon, J. E. & Friesen, W. B. Petrology of Submarine Lavas from Kilauea's Puna Ridge, Hawaii. *Journal of Petrology* **36**, 299–349 (1995).

8. Vinet, N. & Higgins, M. D. Magma Solidification Processes beneath Kilauea Volcano, Hawaii: a Quantitative Textural and Geochemical Study of the 1969-1974 Mauna Ulu Lavas. *Journal of Petrology* **51**, 1297–1332 (2010).
9. Welsch, B., Hammer, J. & Hellebrand, E. Phosphorus zoning reveals dendritic architecture of olivine. *Geology* **42**, 867–870 (2014).
10. Natland, J. H. Capture of Helium and Other Volatiles during the Growth of Olivine Phenocrysts in Picritic Basalts from the Juan Fernandez Islands. *Journal of Petrology* **44**, 421–456 (2003).
11. Wilkinson, J. F. G. & Hensel, H. D. The petrology of some picrites from Mauna Loa and Kilauea volcanoes, Hawaii. *Contributions to Mineralogy and Petrology* **98**, 326–345 (1988).
12. Wright, T. L. & Fiske, R. S. Origin of the Differentiated and Hybrid Lavas of Kilauea Volcano, Hawaii. *Journal of Petrology* **12**, 1–65 (1971).
13. Clague, D. A., Weber, W. & Dixon, J. Picritic Glasses from Hawaii. *Nature* **353**, 6344 (1991).
14. Garcia, M. O. A Petrologic Perspective of Kilauea Volcano's Summit Magma Reservoir. *Journal of Petrology* **44**, 2313–2339 (2003).
15. Clague, D. A. & Denlinger, R. P. Role of olivine cumulates in destabilizing the flanks of Hawaiian volcanoes. *Bulletin of Volcanology* **56**, 425–434 (1994).
16. Park, J. *et al.* Comparative velocity structure of active Hawaiian volcanoes from 3-D onshore–offshore seismic tomography. *Earth and Planetary Science Letters* **259**, 500–516 (2007).
17. Denlinger, R. P. & Morgan, J. K. Instability of Hawaiian Volcanoes. in *Characteristics of Hawaiian Volcanoes* vol. 1801 149–176 (2014).

18. Poland, M. P., Miklius, A. & Emily, M.-B. Magma Supply, Storage, and Transport at Shield-Stage Hawaiian Volcanoes. in *Characteristics of Hawaiian Volcanoes* vol. 1081 179–234 (2014).
19. Cordier, P. Dislocations and Slip Systems of Mantle Minerals. *Reviews in Mineralogy and Geochemistry* **51**, 137–179 (2002).
20. Ave'Lallemant, H. G. & Carter, N. L. Syntectonic Recrystallization of Olivine and Modes of Flow in the Upper Mantle. *Geological Society of America Bulletin* **81**, 2203 (1970).
21. Katayama, I., Jung, H. & Karato, S. New type of olivine fabric from deformation experiments at modest water content and low stress. *Geology* **32**, 1045 (2004).
22. Zhang, S. & Karato, S. lattice preferred orientation of olivine aggregates deformed in simple shear. *Nature* **375(6534)**, 774 (1995).
23. Jung, H. & Karato, S. Water-Induced Fabric Transitions in Olivine. *Science* **293**, 1460–1463 (2001).
24. Karato, S., Jung, H., Katayama, I. & Skemer, P. Geodynamic Significance of Seismic Anisotropy of the Upper Mantle: New Insights from Laboratory Studies. *Annual Review of Earth and Planetary Sciences* **36**, 59–95 (2008).
25. Lloyd, G. E., Farmer, A. B. & Mainprice, D. Misorientation analysis and the formation and orientation of subgrain and grain boundaries. *Tectonophysics* **279**, 55–78 (1997).
26. Prior, D. J. *et al.* The application of electron backscatter diffraction and orientation contrast imaging in the SEM to textural problems in rocks. *American Mineralogist* **84**, 1741–1759 (1999).

27. Bradshaw, R. W., Kent, A. J. R. & Tepley, F. J. Chemical fingerprints and residence times of olivine in the 1959 Kilauea Iki eruption, Hawaii: Insights into picrite formation. *American Mineralogist* **103**, 1812–1826 (2018).
28. Vinet, N., Flemming, R. L. & Higgins, M. D. Crystal structure, mosaicity, and strain analysis of Hawaiian olivines using in situ X-ray diffraction. *American Mineralogist* **96**, 486–497 (2011).
29. Sakyi, P. A., Tanaka, R., Kobayashi, K. & Nakamura, E. Inherited Pb isotopic records in olivine antecryst-hosted melt inclusions from Hawaiian lavas. *Geochimica et Cosmochimica Acta* **95**, 169–195 (2012).
30. Kohlstedt, D. L., Goetze, C. & vander Sande, J. New Technique for Decorating Dislocations in Olivine. *Science* **191**, 1045–1046 (1976).
31. Humphreys, F. J. Review Grain and subgrain characterisation by electron backscatter diffraction. *Journal of materials science* **36(16)**, 3833–3854 (2001).
32. Hansen, L. N., Zhao, Y.-H., Zimmerman, M. E. & Kohlstedt, D. L. Protracted fabric evolution in olivine: Implications for the relationship among strain, crystallographic fabric, and seismic anisotropy. *Earth and Planetary Science Letters* **387**, 157–168 (2014).
33. Larsen, L. M. & Pedersen, A. K. Processes in High-Mg, High-T Magmas: Evidence from Olivine, Chromite and Glass in Palaeogene Picrites from West Greenland. *Journal of Petrology* **41**, 1071–1098 (2000).
34. Wieser, P. E. *et al.* To sink, swim, twin, or nucleate: A critical appraisal of crystalaggregation processes. *Geology* (2019) doi:10.1130/G46660.1.
35. Lockwood, J. P. *et al.* Magma Migration and Resupply During the 1974 Summit Eruptions of Kilauea Volcano, Hawai'i. in *USGS Geological Survey Professional Paper* vol. 1613 47 (1999).

36. Lynn, K. J., Garcia, M. O., Shea, T., Costa, F. & Swanson, D. A. Timescales of mixing and storage for Keanakākoʻi Tephra magmas (1500–1820 C.E.), Kīlauea Volcano, Hawaiʻi. *Contributions to Mineralogy and Petrology* **172**, (2017).
37. Rowland, S. K. & Munro, D. C. The 1919-1920 eruption of Mauna Iki, Kilauea: chronology, geologic mapping, and magma transport mechanisms. *Bulletin of Volcanology* **55**, 190–203 (1993).
38. Garcia, M. O., Rhodes, J. M., Trusdell, F. A. & Pietruszka, A. J. Petrology of lavas from the Puu Oo eruption of Kilauea Volcano: III. The Kupaianaha episode (1986-1992). *Bulletin of Volcanology* **58**, 359–379 (1996).
39. Shea, T. *et al.* Phosphorus and aluminum zoning in olivine: contrasting behavior of two nominally incompatible trace elements. *Contrib Mineral Petrol* **174**, 85 (2019).
40. Spandler, C., O'Neill, H. S. C. & Kamenetsky, V. S. Survival times of anomalous melt inclusions from element diffusion in olivine and chromite. *Nature* **447**, 303–306 (2007).
41. Donaldson, C. H. An experimental investigation of olivine morphology. *Contributions to Mineralogy and Petrology* **57**, 187–213 (1976).
42. Bai, Q. & Kohlstedt, D. L. High-temperature creep of olivine single crystals, 2. Dislocation structures. *Tectonophysics* **206(1–2)**, 1–29 (1992).
43. Boioli, F., Carrez, P., Cordier, P., Devincere, B. & Marquille, M. Modeling the creep properties of olivine by 2.5-dimensional dislocation dynamics simulations. *Physical Review B* **92**, (2015).
44. Thompson, R. N. & Gibson, S. A. Transient high temperatures in mantle plume heads inferred from magnesian olivines in Phanerozoic picrites. *Nature* **407**, 502–506 (2000).

45. Montgomery-Brown, E. K. *et al.* Spatiotemporal evolution of dike opening and décollement slip at Kīlauea Volcano, Hawai'i. *J. Geophys. Res.* **116**, B03401 (2011).
46. Kirby, S. & Green, H. Dunite Xenoliths from Hualalai Volcano: evidence for mantle diapiric flow beneath the island of Hawaii. *American Journal of Science* **280**, 550–575 (1980).
47. Boudier, F. Olivine xenocrysts in picritic magmas: An experimental and microstructural study. *Contributions to Mineralogy and Petrology* **109**, 114–123 (1991).
48. Francis, D. The Baffin Bay lavas and the value of picrites as analogues of primary magmas. *Contr. Mineral. and Petrol.* **89**, 144–154 (1985).
49. Westland, J. The field relationships and mineral chemistry of mafic and ultramafic intrusions in the Loch Uisg area, Isle of Mull. (University of Glasgow, 2014).
50. Hughes, C. *Igneous Petrology*. vol. 7 (Elsevier, 2013).
51. Cao, Y. *et al.* Plastic Deformation and Seismic Properties in Fore-arc Mantles: A Petrofabric Analysis of the Yushigou Harzburgites, North Qilian Suture Zone, NW China. *Journal of Petrology* **56**, 1897–1944 (2015).
52. Toriumi, M. Relation between dislocation density and subgrain size of naturally deformed olivine in peridotites. *Contributions to Mineralogy and Petrology* **68**, 181–186 (1979).
53. Hansen, L. N. & Warren, J. M. Quantifying the effect of pyroxene on deformation of peridotite in a natural shear zone: Pyroxene and peridotite deformation. *Journal of Geophysical Research: Solid Earth* **120**, 2717–2738 (2015).

54. Sides, I. R., Edmonds, M., Maclennan, J., Swanson, D. A. & Houghton, B. F. Eruption style at Kīlauea Volcano in Hawai'i linked to primary melt composition. *Nature Geoscience* **7**, 464–469 (2014).
55. Hauri, E., Gaetani, G. & Green, T. Partitioning of water during melting of the Earth's upper mantle at H₂O-undersaturated conditions. *Earth and Planetary Science Letters* **248**, 715–734 (2006).
56. Jung, H., Katayama, I., Jiang, Z., Hiraga, T. & Karato, S. Effect of water and stress on the lattice-preferred orientation of olivine. *Tectonophysics* **421**, 1–22 (2006).
57. Neave, D. A., Maclennan, J., Hartley, M. E., Edmonds, M. & Thordarson, T. Crystal Storage and Transfer in Basaltic Systems: the Skuggafjöll Eruption, Iceland. *Journal of Petrology* **55**, 2311–2346 (2014).
58. Lange, R. A. & Carmichael, I. S. E. Densities of Na₂O-K₂O-CaO-MgO-FeO-Fe₂O₃-Al₂O₃-TiO₂-SiO₂ liquids: New measurements and derived partial molar properties. *Geochimica et Cosmochimica Acta* **51**, 2931–2946 (1987).
59. Antony, S. J. Link between single-particle properties and macroscopic properties in particulate assemblies: role of structures within structures. *Philosophical Transactions of the Royal Society A: Mathematical, Physical and Engineering Sciences* **365**, 2879–2891 (2007).
60. Bergantz, G. W., Schleicher, J. M. & Burgisser, A. On the kinematics and dynamics of crystal-rich systems: Hydrogranular Dynamics. *Journal of Geophysical Research: Solid Earth* **122**, 6131–6159 (2017).
61. Sperl, M. Experiments on corn pressure in silo cells – translation and comment of Janssen's paper from 1895. *Granular Matter* **8**, 59–65 (2006).

62. Tordesillas, A., Walker, D. M. & Lin, Q. Force cycles and force chains. *Phys. Rev. E* **81**, 011302 (2010).
63. Estep, J. & Dufek, J. Substrate effects from force chain dynamics in dense granular flows. *Journal of Geophysical Research: Earth Surface* **117(F1)**, (2012).
64. Gallagher, J., Friedman, M., Handin, J. & Sowers, G. Experimental Studies Relating to Microfracture in Sandstone. *Tectonophysics* **21(3)**, 203–247 (1974).
65. Wheeler, J. The effects of stress on reactions in the Earth: Sometimes rather mean, usually normal, always important. *Journal of Metamorphic Geology* **36**, 439–461 (2018).
66. Cervelli, P. F. & Miklius, A. The Shallow Magmatic System of Kīlauea Volcano. in *USGS professional paper vol. 1676* 149–163 (2003).
67. Pietruszka, A. J., Marske, J. P., Heaton, D. E., Garcia, M. O. & Rhodes, J. M. An Isotopic Perspective into the Magmatic Evolution and Architecture of the Rift Zones of Kīlauea Volcano. *Journal of Petrology* (2018)
doi:10.1093/petrology/egy098.
68. Pietruszka, A. J., Heaton, D. E., Marske, J. P. & Garcia, M. O. Two magma bodies beneath the summit of Kīlauea Volcano unveiled by isotopically distinct melt deliveries from the mantle. *Earth and Planetary Science Letters* **413**, 90–100 (2015).
69. Helz, R. T., Clague, D. A., Mastin, L. G. & Rose, T. R. Evidence for Large Compositional Ranges in Coeval Melts Erupted from Kīlauea’s Summit Reservoir. in *Hawaiian Volcanoes: from source to surface* 125–145 (2015).
70. Wieser, P. E., Edmonds, M., Maclennan, J., Jenner, F. E. & Kunz, B. E. Crystal Scavenging from Mush Piles Recorded by Melt Inclusions. *Nature Communications* (In press.).

71. Anderson, K. R. & Poland, M. P. Bayesian estimation of magma supply, storage, and eruption rates using a multiphysical volcano model: Kīlauea Volcano, 2000–2012. *Earth and Planetary Science Letters* **447**, 161–171 (2016).
72. Baker, S. & Amelung, F. Top-down inflation and deflation at the summit of Kīlauea Volcano, Hawai'i observed with InSAR. *Journal of Geophysical Research: Solid Earth* **117**, (2012).
73. Davidson, J., Turner, S., Handley, H., Macpherson, C. & Dosseto, A. Amphibole “sponge” in arc crust? *Geology* **35**, 787 (2007).
74. Cashman, K. V., Sparks, R. S. J. & Blundy, J. D. Vertically extensive and unstable magmatic systems: A unified view of igneous processes. *Science* **355**, eaag3055 (2017).
75. AvéLallemant, H. G. Experimental deformation of diopside and websterite. *Tectonophysics* **48**, 1–27 (1978).
76. Stünitz, H., Fitz Gerald, J. D. & Tullis, J. Dislocation generation, slip systems, and dynamic recrystallization in experimentally deformed plagioclase single crystals. *Tectonophysics* **372**, 215–233 (2003).
77. Ko, B. & Jung, H. Crystal preferred orientation of an amphibole experimentally deformed by simple shear. *Nat Commun* **6**, 6586 (2015).
78. Bachmann, F., Hielscher, R. & Schaeben, H. Texture Analysis with MTEX – Free and Open Source Software Toolbox. *Solid State Phenomena* **160**, 63–68 (2010).
79. Brough, I., Bate, P. S. & Humphreys, F. J. Optimising the angular resolution of EBSD. *Materials Science and Technology* **22**, 1279–1286 (2006).
80. Prior, D. Problems in determining the misorientation axes, for small angular misorientations, using electron backscatter diffraction in the SEM. *J Microsc* **195**, 217–225 (1999).

81. Wheeler, J., Prior, D., Jiang, Z., Spiess, R. & Trimby, P. The petrological significance of misorientations between grains. *Contributions to Mineralogy and Petrology* **141**, 109–124 (2001).
82. Wheeler, J. *et al.* The weighted Burgers vector: a new quantity for constraining dislocation densities and types using electron backscatter diffraction on 2D sections through crystalline materials. *Journal of Microscopy* **233**, 482–494 (2009).
83. Ryan, W. B. F. *et al.* Global Multi-Resolution Topography synthesis. *Geochem. Geophys. Geosyst.* **10**, n/a-n/a (2009).
84. Moussallam, Y. *et al.* The impact of degassing on the oxidation state of basaltic magmas: A case study of Kīlauea volcano. *Earth and Planetary Science Letters* **450**, 317–325 (2016).
85. Roeder, P. L. & Emslie, R. F. Olivine-liquid equilibrium. *Contributions to Mineralogy and Petrology* **29**, 275–289 (1970).
86. Matzen, A. K., Baker, M. B., Beckett, J. R. & Stolper, E. M. Fe–Mg Partitioning between Olivine and High-magnesian Melts and the Nature of Hawaiian Parental Liquids. *Journal of Petrology* **52**, 1243–1263 (2011).

Figures

Fig. 1 |

Location of eruptions examined in this study.

a) Map of the Hawaiian Island Chain, with the red rectangle showing the location of Kīlauea Volcano on the island of Hawai'i (expanded in part **b**). **b)** Expanded map of Kīlauea Volcano, with colored symbols showing the location of eruption deposits examined in this study (symbol colors and shapes are the same as those used in Fig. 5). The East Rift Zone (ERZ), and volcanic and seismic strand of the South West Rift Zone (VSWRZ and SSWRZ respectively)

are shown in black dashed lines. **c)** Schematic histogram representing the proportion of distorted grains in 3 size categories (all grains, grains >1 mm and <1 mm based on sieved size fractions). For each eruption site, a colored histogram following this schematic shows the proportion of distorted grains in each size category. The number of distorted (N_D) and undistorted (N_U) grains is also shown, along with the symbol used on the basemap. Basemap from GEOMAPP APP (ref. ⁸³; <http://www.geomapp.org>), showing the topography of Kīlauea before the onset of the 2018 summit collapse.

Fig. 2 |

Relationships between minor element enrichments and lattice distortions. Wavelength dispersive spectrometry (WDS) maps of P enrichment compared to electron back-scatter diffraction (EBSD) maps (scale for both images shown on EBSD map). **a-c)** Grains with internal lattice distortions (revealed by stripes of different colors in EBSD maps) have homogenous concentrations of P in their cores (see WDS maps). Observed phosphorus enrichments in the rim of the crystal shown in part **c** mark a period of rapid growth upon eruption. **d)** Internal P enrichments are truncated against a subgrain boundary. WDS elemental maps are colored by the number of counts per pixel (in ImageJ). EBSD maps are colored using the inverse pole figure (IPF) key. A color reference direction is chosen such that the mean orientation of the central grain is colored white. The coloring denotes the misorientation axis and angle of each pixel relative to this reference direction. To emphasize small misorientations, the IPF key has been shrunk so that all the color variation is distributed across misorientation angles of 0-3°. For example, pixels misoriented about [010] by 3 degrees from the mean orientation are colored dark blue (see the color scale, top right). Pixels misorientated by >3° are colored black. Light blue 3D olivine crystals are superimposed (using the MTEX crystalShape package) to allow visualization of the orientation of the three crystallographic axes ([100], [010], and [001], for space group Pbnm).

Fig. 3 |

Crystallographic signatures of dendritic branching in olivines from West Greenland Picrites.

a) Electron backscatter diffraction (EBSD) maps colored using the inverse pole figure (IPF) key as in Fig. 2, with the mean orientation of the grain containing the red dot set to white. To emphasize the larger range of misorientation in dendrite branches compared with the distorted olivines in Fig. 2, the IPF color key was adjusted so that pixels with deviation angles >20° are colored black. 3D olivine crystals are overlain to allow visualization of the orientation of the dendritic olivines with respect to the three crystallographic directions of olivine. **b)** Weighted

Burgers Vector directions (WBVDs) overlain on band contrast maps ([100]=green, [010]=blue, [001]=red]). Scale for both images shown on EBSD map. **c)** Misorientation axes for 125 dendritic buds from West Greenland picrites (misorientation angle $>1^\circ$). The color scale has units of 'multiples of uniform distribution'. **d)** Histogram of misorientation angles between adjacent dendrite buds. 70% of dendritic buds are misoriented from the host crystal by $>5^\circ$ (see ref. ³⁴).

Fig. 4 |

Crystallographic signatures of lattice distortions within Kīlauean olivines.

a) Electron backscatter diffraction (EBSD) maps colored using the inverse pole figure (IPF) key as in Fig. 2 (scaled to 3°). 3D olivine shapes are overlain to demonstrate the average orientation of the olivine crystal with respect to the three crystallographic axes. **b)** Weighted Burgers Vector directions (WBVDs) overlain on band contrast maps ([100]=green, [010]=blue, [001]=red]). Scale for both images shown on EBSD map. **c)** Misorientation axes across subgrain boundaries located within the red box indicated in column **a**. The color scale has units of 'multiples of uniform distribution'. Subgrain boundaries with [100] WBVDs (green) show misorientation axes between [001] and [010]. Subgrain boundaries with [001] WBVDs (red) show misorientation axes about [100] or [010].

Fig. 5 |

Chemical differences between deformed and undeformed Kīlauean olivine grains.

a-b) Olivine forsterite contents (mol %) versus matrix glass Mg# ($Fe^{3+}/Fe_T=0.15$; ~QFM; ref. ⁸⁴). Olivine-liquid equilibrium lines are shown for $K_D=0.270-0.352$ (refs. ^{85,86}). Both deformed and undeformed grains have higher forsterite contents than the equilibrium olivine composition of their matrix glasses. However, deformed grains show a narrower range of forsterite contents, which lie further from the equilibrium field than undeformed grains. **c-f)** Cumulative distribution functions comparing undeformed (solid lines) and deformed (dashed lines) olivines for 4 eruptions. Deformed grains are more primitive at a statistically significant level ($p<0.01$) using the two sample Kolmogorov-Smirnov test. The test statistic D (representing the distance between the two distributions) is also shown. SSWRZ – seismic South West Rift Zone, VSWRZ – volcanic South West Rift Zone.

Fig. 6 |

Textural and chemical evolution during downslope flow.

a) CaO contents of deformed Kīlauean olivines (excluding the ~1700 AD lava flow) plot well outside the field for mantle olivines (ref. ⁴⁴), and have substantially higher CaO contents than olivines from Hualalai dunites (ref. ¹⁵). Some deformed olivines from ~1700 AD have lower CaO contents than undeformed olivines in this sample. In fact, three deformed olivines fall within the field of Hualalai dunites. **b)** Backscatter electron image showing prominent melt films along high angle boundaries (yellow lines) in the interior of a deformed crystal from the ~1700 AD eruption. **c)** Electron backscatter diffraction (EBSD) map colored with the inverse pole figure (IPF) colour key scaled to 10° about the mean orientation of the central grain. High angle boundaries (misorientation angle >10°) are colored yellow, and low angle boundaries (misorientation angle <10°) are colored black. Scale for both images shown on the backscatter image.

Fig. 7 |

Slip system identification method developed for this study.

a) A schematic diagram of a tilt boundary, where the misorientation axis lies within the plane of the low angle boundary. **b)** A schematic diagram of a twist boundary, where the boundary plane is perpendicular to the misorientation axis. Two sets of screw dislocations are shown within the twist wall for illustrative purposes; this is just one possible geometry. **c)** Map of Weighted Burgers Vector directions (WBVDs) in a deformed olivine. Specimen coordinates (orange arrows) represent the x, y, and z directions within the scanning electron microscope. Crystal coordinates (pink arrows) represent the directions of the [100], [010], and [001] axes of the olivine. A 3D olivine crystal is overlain to demonstrate the orientation of the crystal in crystal co-ordinates. Boundaries with [100] WBVDs are almost parallel to the y direction, while those with [001] WBVDs are almost parallel to the x direction in specimen coordinates. A small section of a [100] WBVD boundary is selected for further discussion (pink rectangle). **d)** Ideal tilt (yellow) and twist (red) boundaries calculated for each boundary segment in the pink rectangle based on the trace of the subgrain boundary and direction of the misorientation axis (in specimen coordinates). As the calculated twist wall planes show extremely low dips, the MTEX code classifies all segments along this boundary as tilt walls. **e)** Schematic diagram showing the misorientation axes in crystal coordinates for tilt boundaries built from dislocation types associated with each of the 5 olivine slip systems (written as (slip plane)[Burgers vector]), allowing 20° leniency. Misorientation axes of the boundary pixels within the pink rectangle plot near [010]. Along with the [100] WBVDs, this indicates that this tilt wall consists of (001)[100] dislocations.

Fig. 8 |

Quantifying the conditions of deformation.

a) Proportions of each slip system calculated by averaging the proportion of each slip system per grain (darker colors; giving equal weight to all grains regardless of their size), and by summing the total length of each boundary type in 62 deformed grains (lighter colors). All deformed grains contain [100] Weighted Burgers Vector directions (WBVDs), suggesting that this is the primary slip direction. Only a subset of grains contain low angle boundaries with [001] WBVDs, suggesting that this is a secondary slip direction. **b)** Differential stresses calculated using subgrain piezometry (ref. ⁵²) applied to linear intercept distances clearly overlap with those estimated from dislocation density piezometry (ref. ⁴²) on published dislocation densities (ref. ²⁹). Differential stress estimates are shown as a cumulative density function (CDF – magenta) with the interquartile range in light pink (IQR), and as a histogram (darker blue). **c)** Olivine regime diagram (ref. ⁵⁶) for T=1470–1570 K with subgrain stress estimates (purple bar) and olivine water contents (orange bar) superimposed.

Fig. 9 |

Schematic cross section along the magmatic plumbing system of Kīlauea diagram showing the formation of deformed olivines.

a) Olivine crystals in intracaldera eruptions thought to tap the shallower reservoir based on Pb isotope compositions (refs. ^{67,68}) are largely undeformed. These crystals have evolved forsterite contents, close to the equilibrium composition of their matrix glasses. Extracaldera and rift eruptions, thought to tap the deeper SC reservoir based on Pb isotopes (refs. ^{67,68}), entrain deformed crystals from melt-rich olivine mush piles at the base of the deeper reservoir just prior to eruption. The Mauna Iki eruption taps a mixed crystal cargo, from the upper and lower reservoir (ref. ³⁷). The ~1700 AD eruption and the Kīlauea Iki eruption (ref. ⁶) may tap olivine bodies that have begun their descent into the deep rift zones. **b)** Schematic diagram of force chains within granular olivine mush piles (adapted from ref. ⁶⁰). Primary members can experience forces ~6x the mean force, secondary members experience less than the mean force, while spectator particles experience no force.

Fig. 10 |

Estimating mush pile accumulation rates using a simple box model.

a) A cylinder is supplied with primary melt (16.5 wt% MgO) at a rate of 0.1km³/yr (ref. ⁷¹). Fractionation of these primary melts to the average whole-rock MgO contents of erupted lavas (~10 wt %) requires fractionation of 14 vol % olivine crystals (ref. ¹⁵). **b)** The play off between cylinder radius and accumulation time is shown for mush piles with thicknesses of 180 m and 720 m (assuming 40% porosity). Available constraints on reservoir radius from interferometric

synthetic aperture radar (InSAR) are shown in yellow (ref. ⁷²). Melt inclusion trace element diversity at Kīlauea indicates that crystals are stored in mush piles for >170 years (ref. ⁷⁰; grey line). These geometric and temporal constraints bracket the range of mush thicknesses estimated in this study.

Acknowledgments

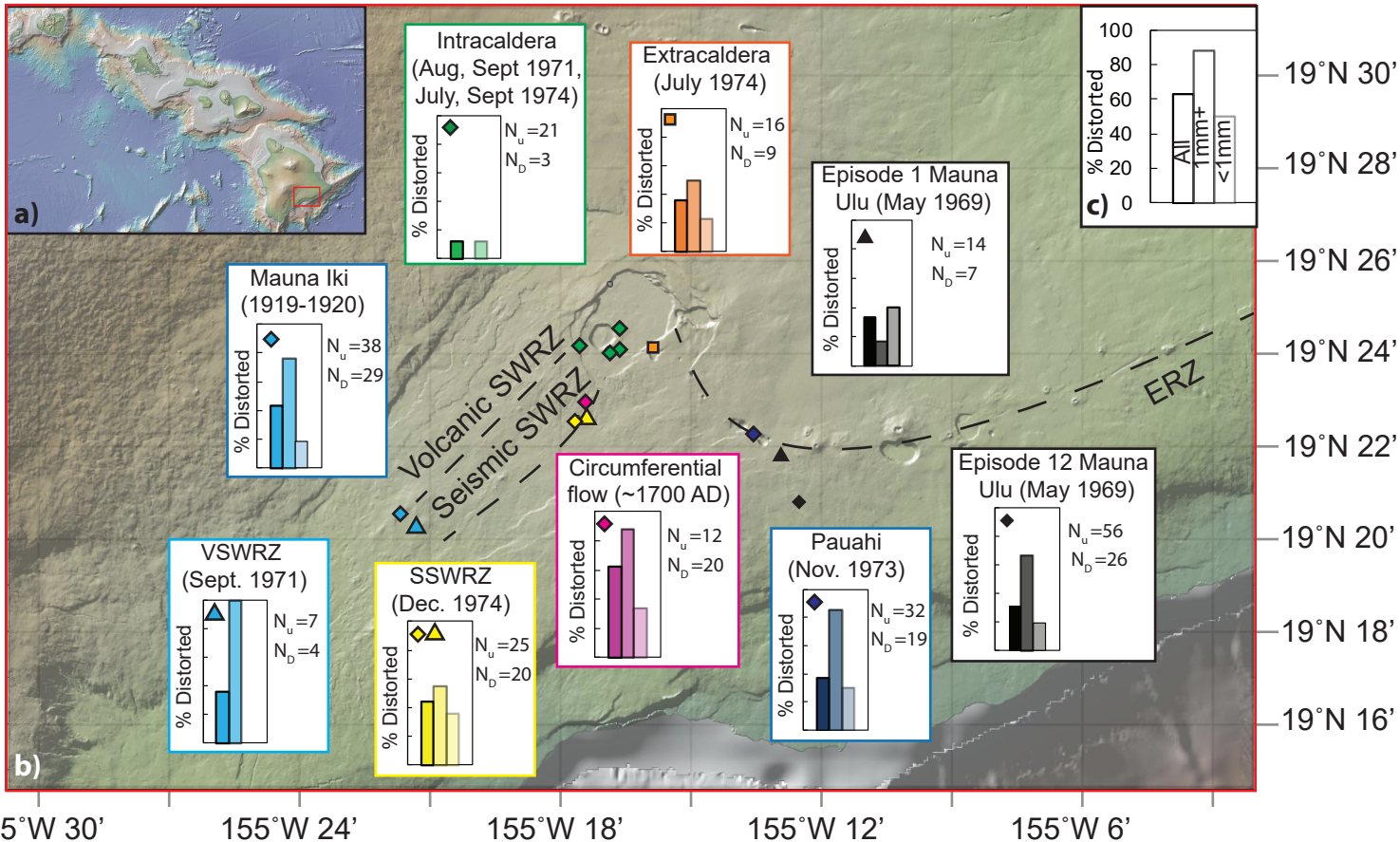
We acknowledge Zoja Vukmanovic, Lars Hansen, and Chris Gregson for very helpful discussions about identifying slip systems. Isobel Sides and Don Swanson collected the Kīlauea samples used in this study, and Lotte Larsen is thanked for providing the Greenland picrite samples. Giulio Lampronti and Iris Buisman are thanked for help collecting EBSD and EPMA data. PW is funded by NERC DTP studentship NE/L002507/1.

Author Contributions

PW conceived the project with help from ME and JM. PW prepared the samples, collected and processed the EBSD and EPMA data and wrote the MTEX code. JW provided the WBVD scripts and guidance interpreting the EBSD data. PW wrote the manuscript with help from ME, JM and JW.

Competing interests

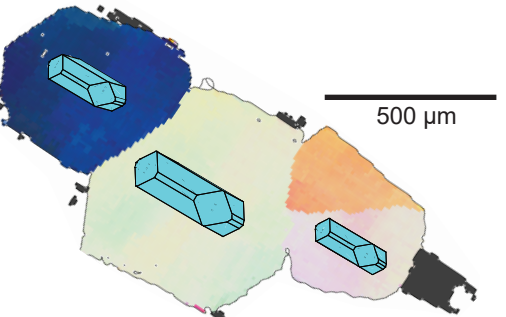
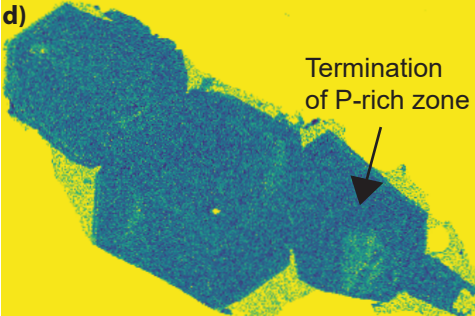
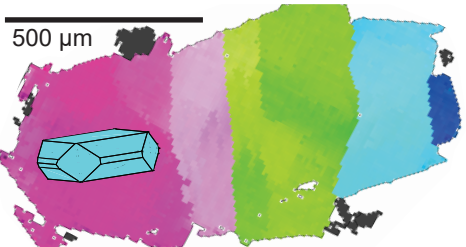
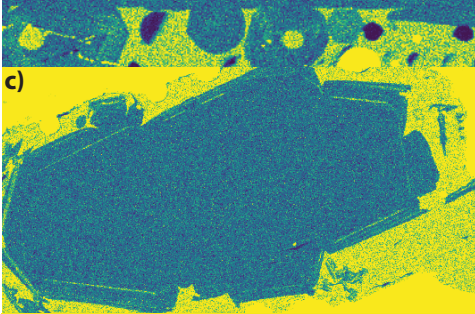
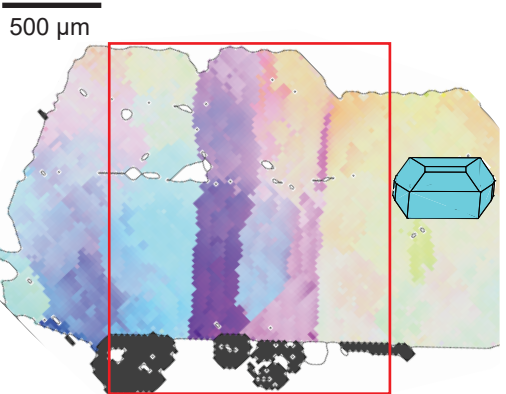
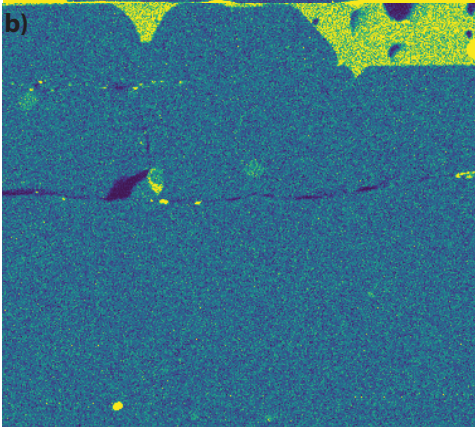
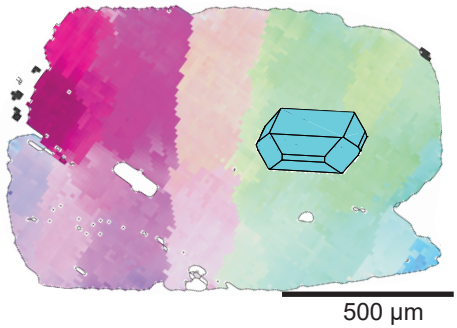
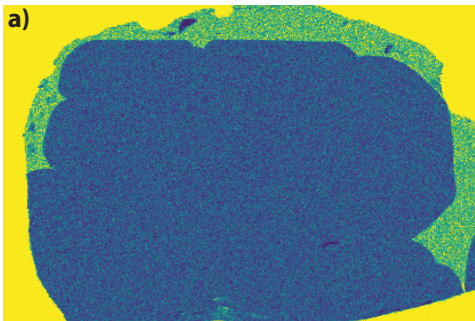
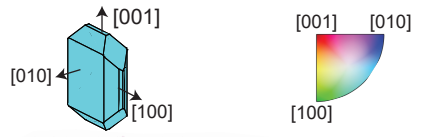
The authors declare no competing interests.

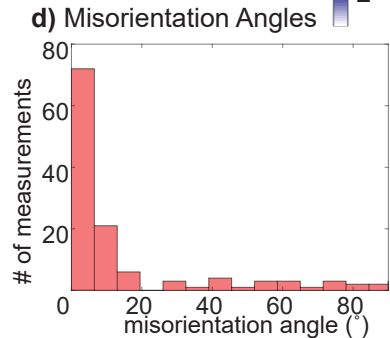
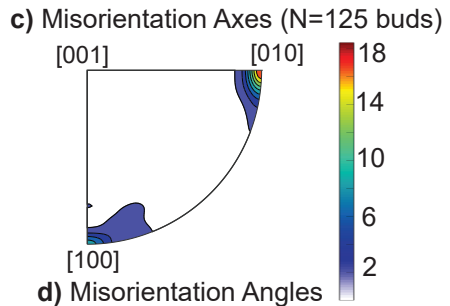
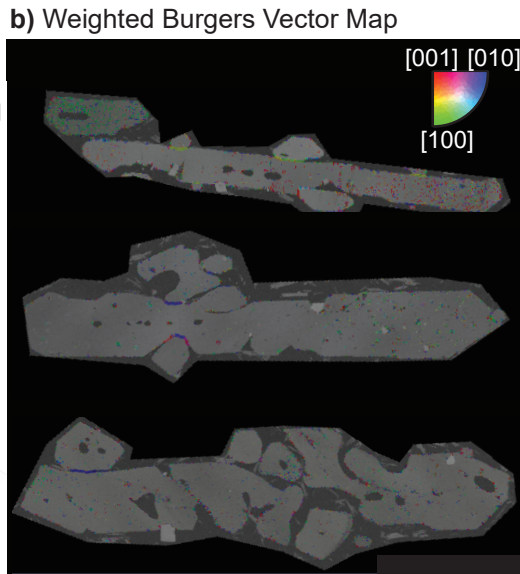
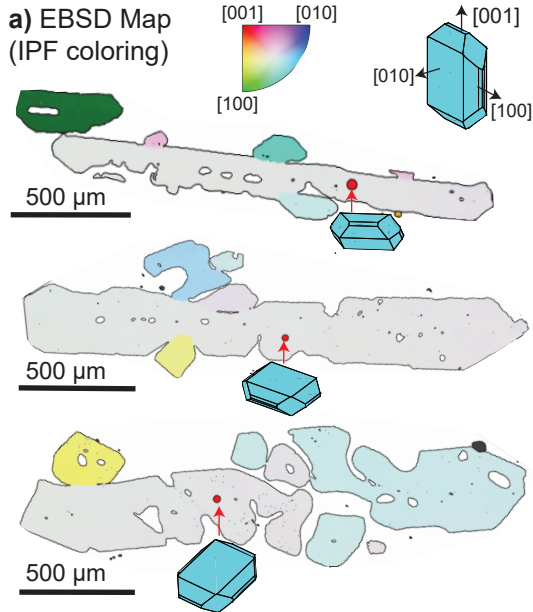


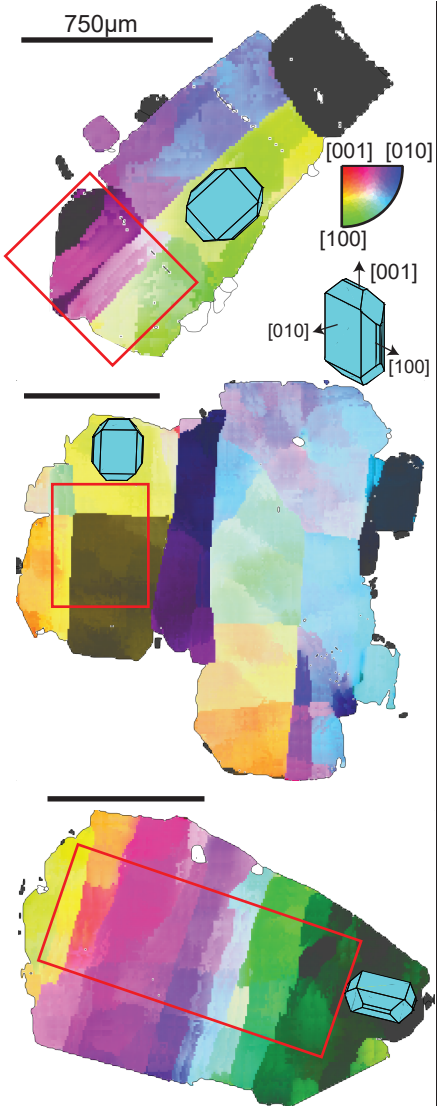
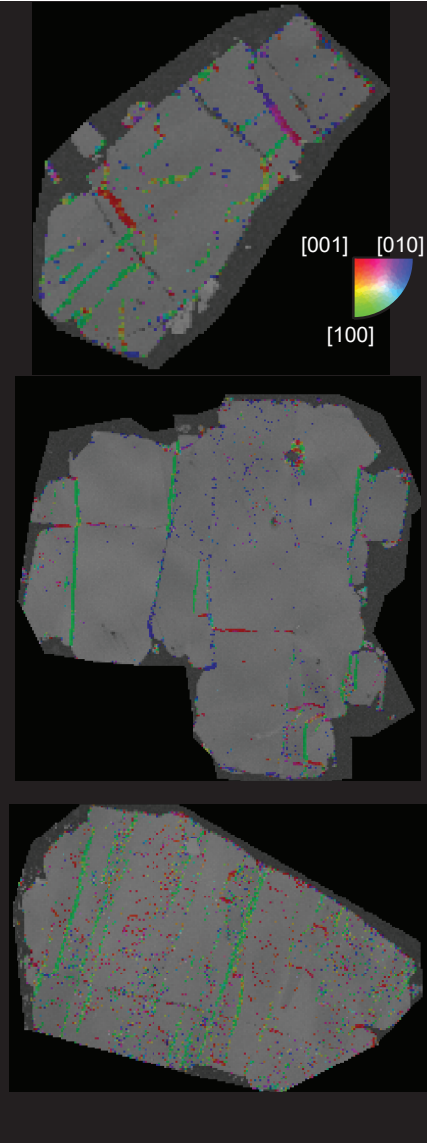
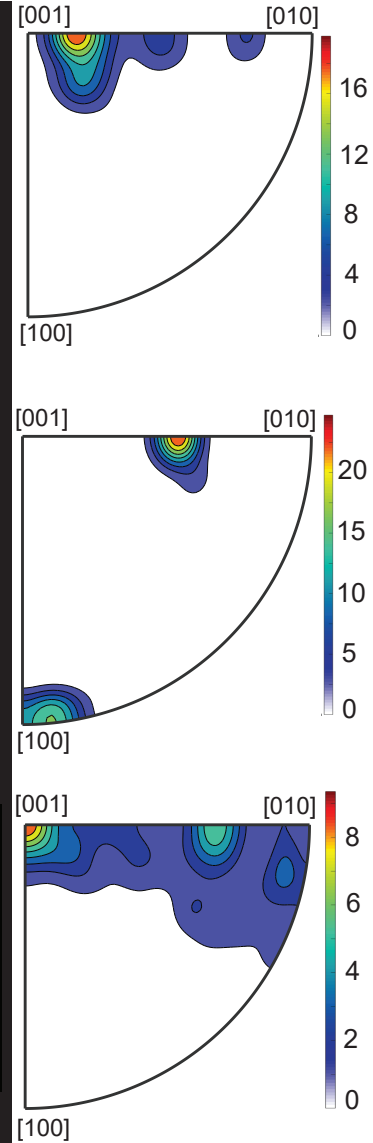
WDS Maps

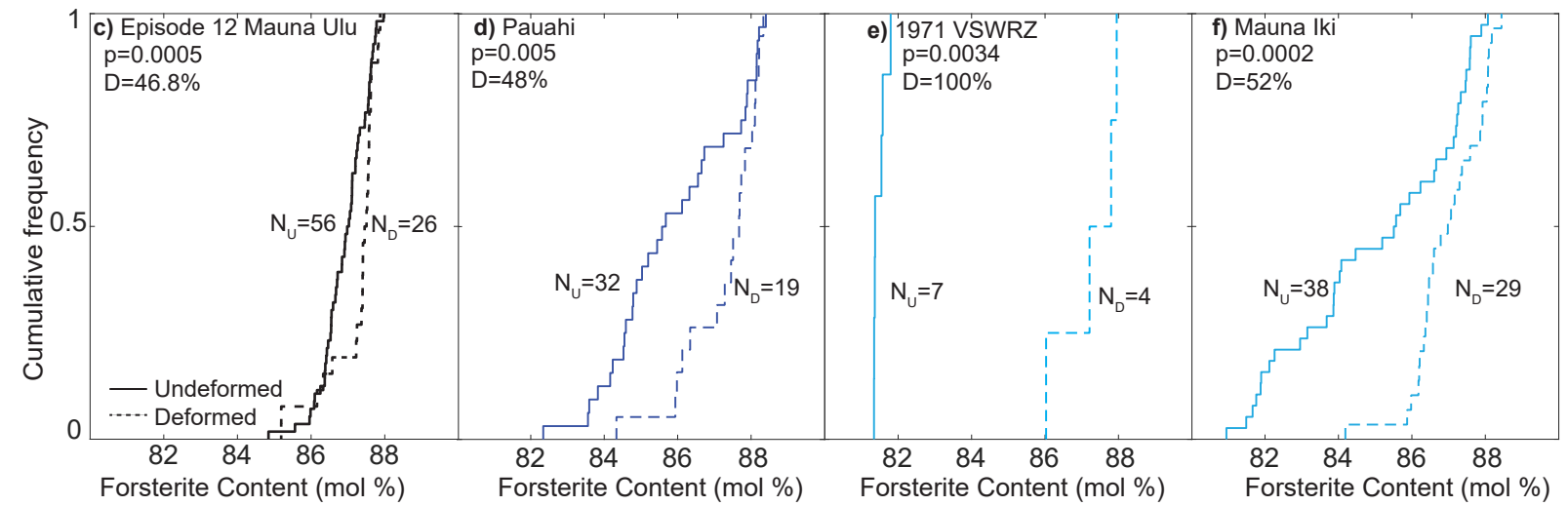
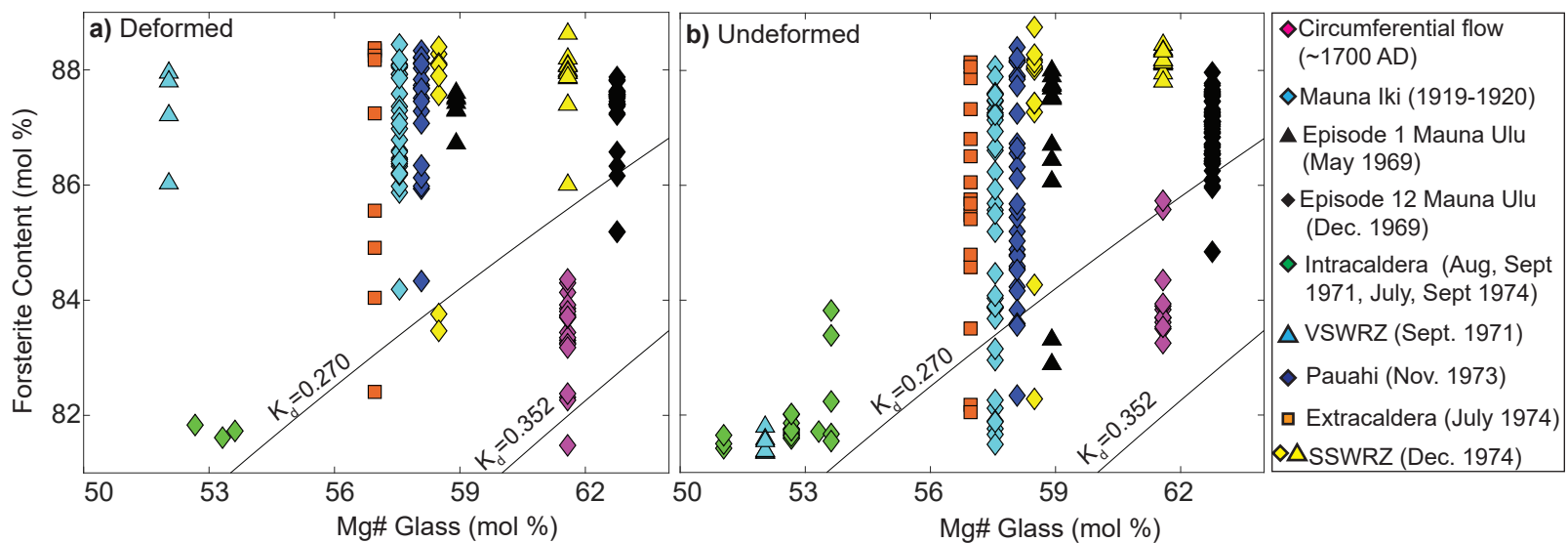


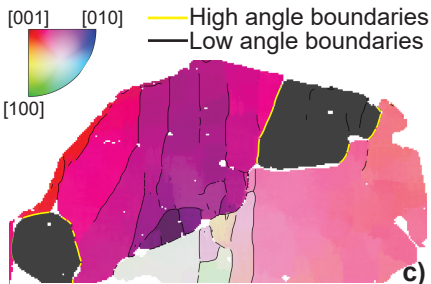
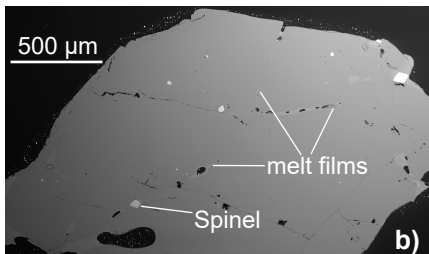
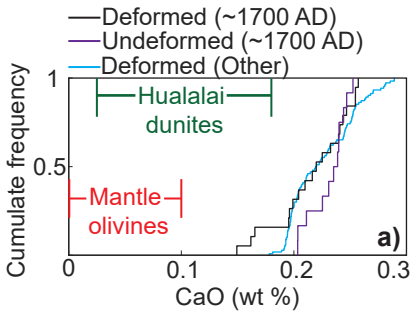
EBSD Maps

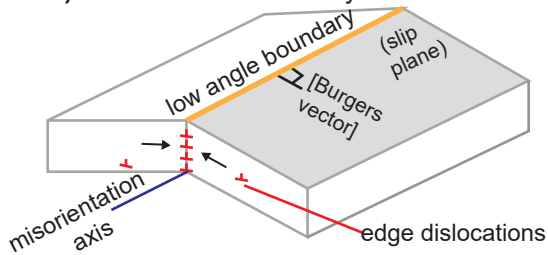
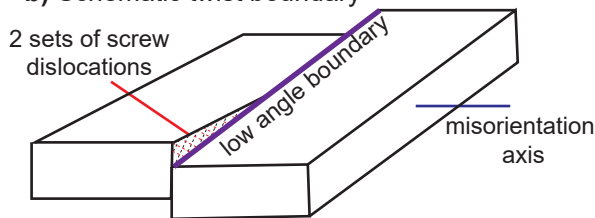
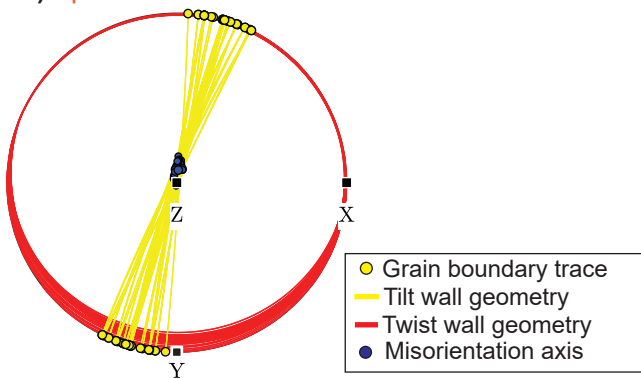
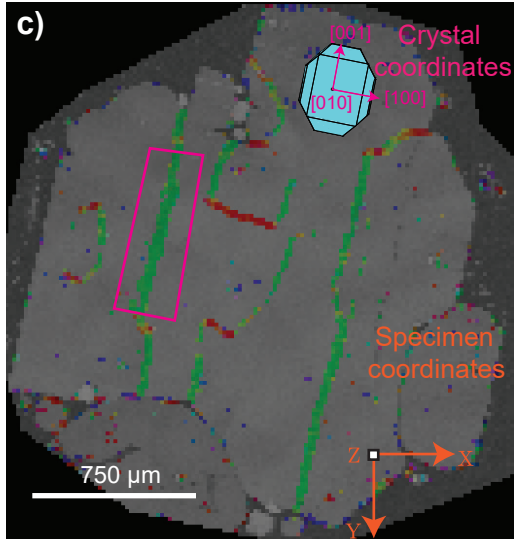
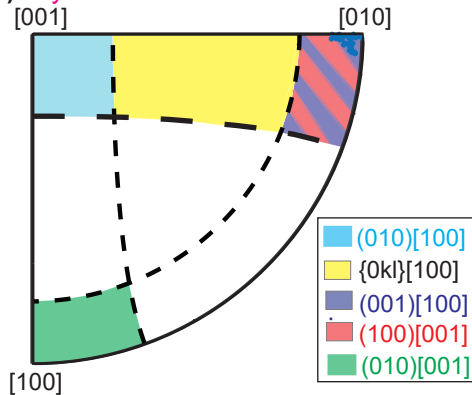


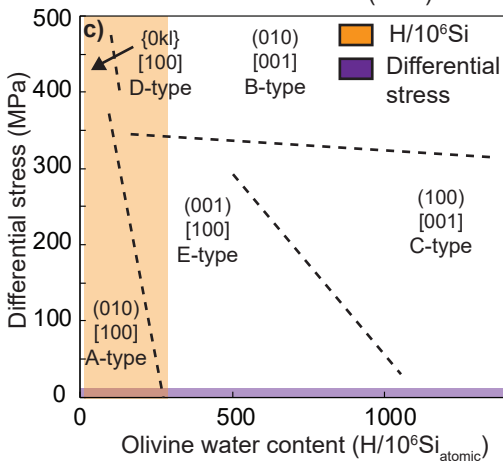
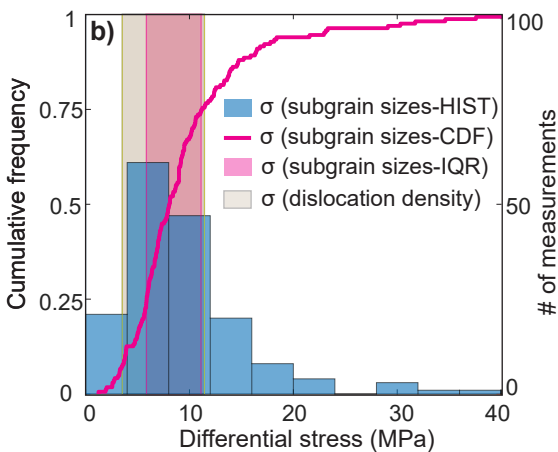
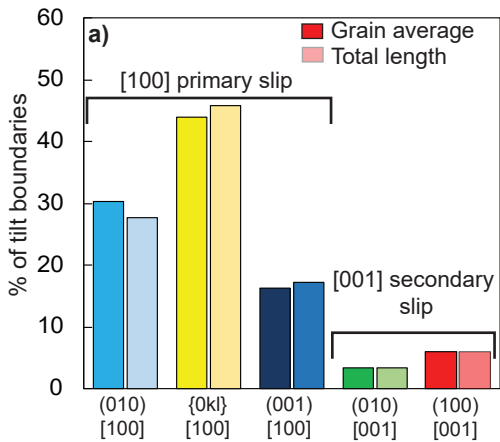


a) EBSD Map (IPF Coloring)**b) Weighted Burgers Vector Map****c) Misorientation Axes**





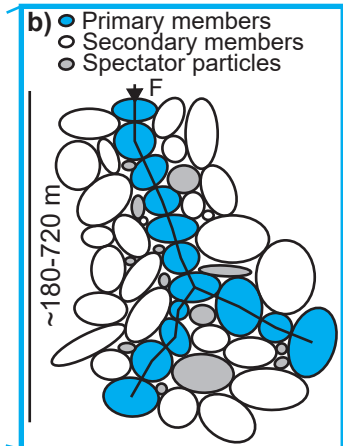
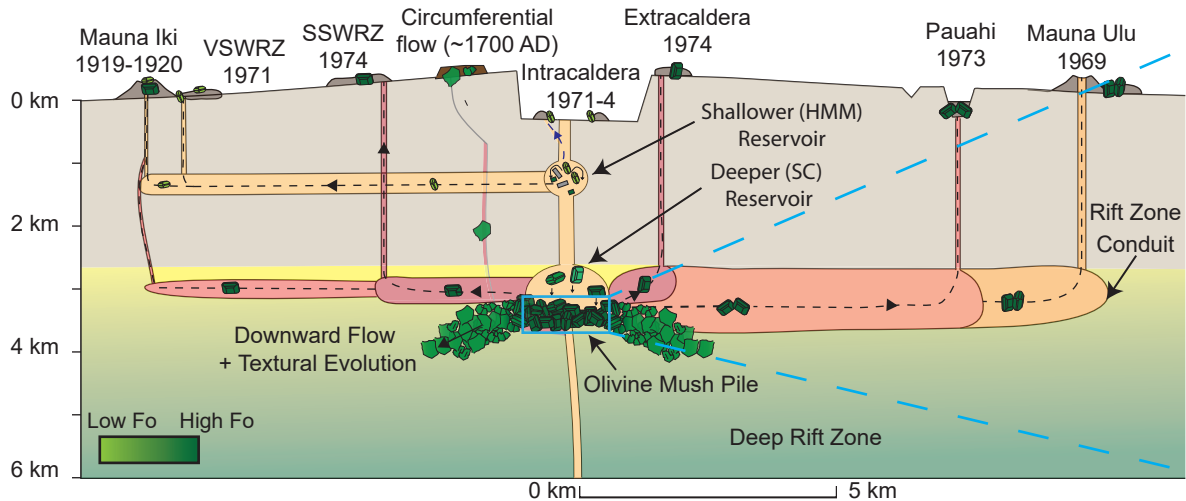
a) Schematic tilt boundary**b) Schematic twist boundary****d) Specimen coordinates****c)****e) Crystal coordinates**

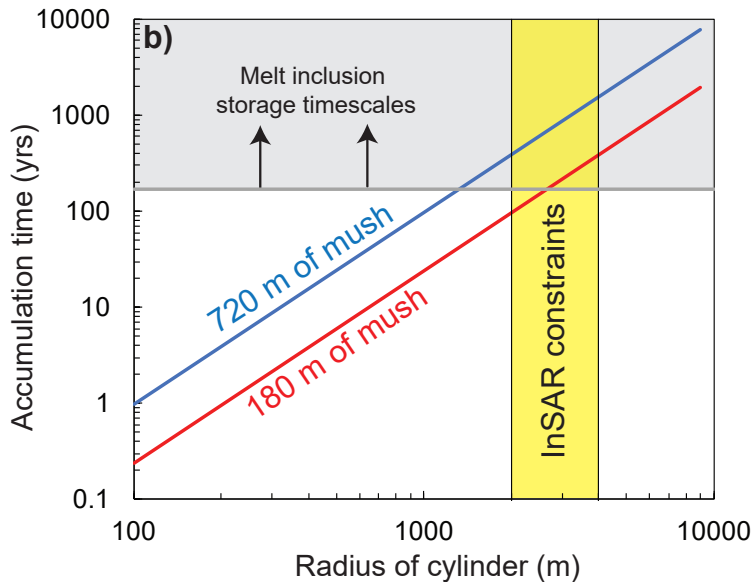
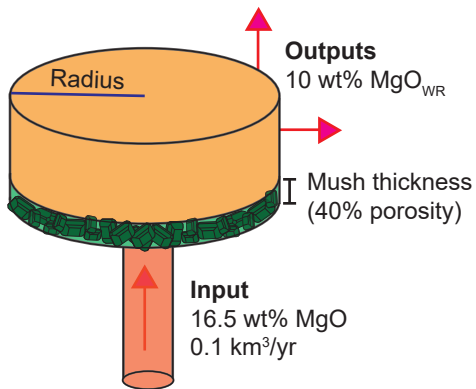
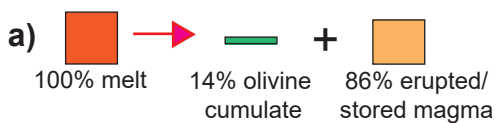


a) South West Rift Zone

Summit Caldera

East Rift Zone





**Supplementary Information: Microstructural Constraints on Magmatic Mushes under
Kīlauea Volcano, Hawai'i**

Penny E. Wieser^{*1}, Marie Edmonds¹, John Maclennan¹ and John Wheeler²

¹ Department of Earth Sciences, University of Cambridge, Downing Street, Cambridge, UK,
CB2 3EQ.

² Department of Earth, Ocean and Ecological Sciences, University of Liverpool.

* Corresponding author: pew26@cam.ac.uk

Supplementary Tables

Supplementary Table 1 – Spatial and temporal information for the samples used in this study.

Sample	Eruption Date	Description	Location	GPS co-ordinates
KL0909	May 24 th , 1969	Ep. 1 Mauna Ulu	ERZ	19° 21.826' N, 155° 12.877' W
KL0908	Dec 30 th , 1969	Ep. 12 Mauna Ulu	ERZ	19° 20.839' N, 155° 12.518' W
KL0910	Nov 10 th , 1973	Pau'ahi Crater	ERZ	19° 22.313' N, 155° 13.510' W
KL0914	Sept 24-29 th , 1971		Intracaldera	19° 24.580' N, 155° 16.631' W
KL0916	Aug 14 th , 1971		Intracaldera	19° 24.137' N, 155° 16.644' W
KL0917	Late July, 1974		Intracaldera	19° 24.06' N, 155° 16.653' W
KL0919	Late Dec, 1974	Ka'u Desert	SSWRZ	19° 22.649' N, 155° 17.609' W
KL0920	Late Dec, 1974	Ka'u Desert	SSWRZ	19° 22.603' N, 155° 17.713' W
KL0921	~1700 AD	Circumferential flow, Ka'u Desert	SSWRZ	19° 22.989' N, 155° 17.464' W
KL0922	Sept 1974		Intracaldera	19° 24.201' N, 155° 17.502' W
KL0924	Late July, 1974		Extracaldera	19° 24.142' N, 155° 16.896' W
KL0930	1919-1920	Mauna Iki	NSWRZ	19° 21.230' N, 155° 23.892' W
KL0931	Sept 24-29 th , 1971		NSWRZ	19° 20.625' N, 155° 21.659' W

Supplementary Table 2 – EBSD acquisition parameters.

SEM Settings		EBSD Settings	
Aperture	3	Sample-Detector Distance	~14 mm
Voltage	20 kV	Background (frames)	2
Beam Size	5.5	Gain	10-30
Sample Tilt	70°	Hough Resolution	60
Working Distance	~17-14 mm	Band Detection (min/max)	Min 6 max 12
Step size (um)	3-15 μ m	Reference	Forsterite (Fe 0.2 MgO 1.8) AMSDB-ID: 0008912
		EBSP resolution	320x240 pixels

Supplementary Table 3 – Calibration materials, count times, and estimates of analytical precision and accuracy for EPMA analysis of olivine crystals. Precision and accuracy was estimated from repeated measurements of a San Carlos Olivine secondary standard. Some instrument drift occurred in session 2. We only report forsterite contents from this session (forsterite contents measured in repeated analyses of San Carlos olivine were used to create a linear interpolation model to correct instrument drift). The drift was less coherent for Si and Ca, so these elements are not reported. Ca contents for run 1 and 3 were internally corrected to the values measured in the San Carlos olivine standard (factors of 1.3 and 1.05 respectively).

Element	Calibration	Crystal	Peak Count time	Analysis order	Condition	Precision (%) (Std dev/mean)	Accuracy (%) (measured / standard)
Session 1 – 30nA, 15kV. November, 2017							
Si	Diopside	TAP	10s	1 st	N/A	0.49	99.0
Mg	St. Johns Olivine	TAP	20s	2 nd	N/A	1.16	97.7
Fe	Fayalite	LIF	20s	1 st	N/A	1.07	99.3
Ca	Diopside	LPET	60s	1 st	N/A	9.3	130.7
Session 1 – February 2018 – Dual condition run Cond1 = 30nA, 15kV; Cond 2 = 100nA, 15kV							
Si	Diopside	TAP	10s	1 st	1	1.12	99.26
Mg	St. Johns Olivine	TAP	20s	2 nd	1	2.41	100.30
Fe	Fayalite	LIF	20s	1 st	1	1.14	98.47
Ca	Diopside	LPET	10s	1 st	2	12.3	118.0
Session 3 –40nA, 15kV. March 2018,							
Si	Diopside	TAP	20s	1 st	N/A	0.67	100.7
Mg	St. Johns Olivine	LTAP	20s	1 st	N/A	0.72	99.9
Fe	Fayalite	LIF	20s	1 st	N/A	0.93	100.58
Ca	Diopside	PET, LPET	30s, 20s	1 st	N/A	0.93	105.4

Supplementary Table 4 - Calibration materials and count times for EPMA analyses of matrix glasses.

Element	Calibration Material	Crystal	Peak Count Time	Analysis order
Na	Jadeite	LTAP	10s	1 st
Al	Corundum	LTAP	20s	2 nd
Ca	Diopside	PET	20s	1 st
P	Apatite	PET	60s	2 nd
K	K feldspar	LPET	10s	1 st
Ti	Rutile	LPET	60s	2 nd
Si	Diopside	TAP	10s	1 st
Mg	St. Johns Olivine	TAP	20s	2 nd

Fe	Fayalite	LIF	20s	1 st
Cr	Cr spinel	LIF	40s	2 nd
Mn	Manganese	LIF	40s	3 rd

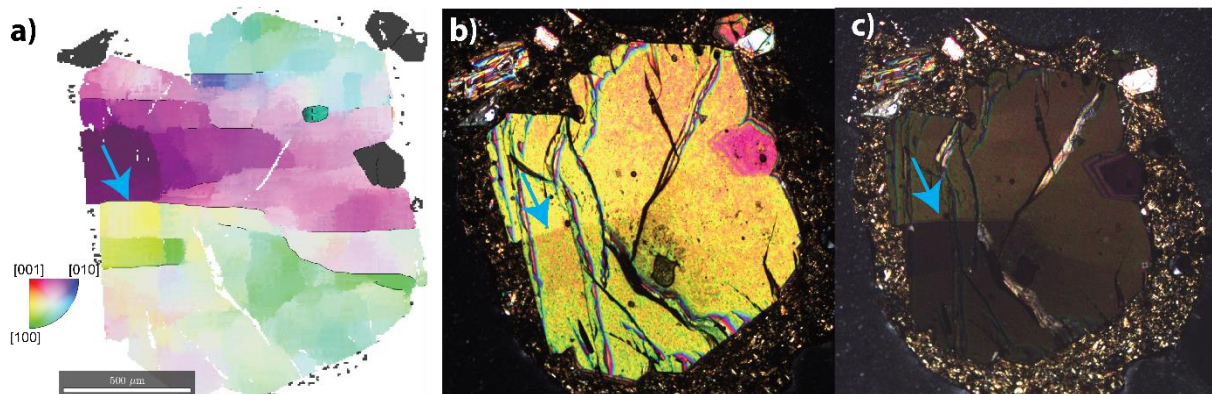
Supplementary Table 5 - Precision and accuracy for EPMA analyses of matrix glasses and melt inclusions. Precision and accuracy was estimated from repeated measurements of VG2 and Basalt_113716-1 secondary standards.

Element	SiO ₂	Mg O	Al ₂ O ₃	Ca O	TiO ₂	FeO	Cr ₂ O 3	MnO	Na ₂ O	K ₂ O	P ₂ O ₅
% Accuracy BCR	98.3	98.3	101. 5	99.2	101. 2	100. 7	279. 5	85.1	101. 9	99. 8	84.9
% Precision BCR	1.5	1.6	1.1	1.7	2.3	2.7	115. 8	15.8	6.4	11. 6	20.6
% Accuracy Indian Ocean Basalt_1137 16-1	99.2	98.5	101. 7	99.0	103. 6	101. 3	108. 8	125. 8	100. 5	91. 0	104. 3
% Precision Indian Ocean Basalt_1137 16-1	1.4	2.2	1.7	1.8	1.8	2.8	66.2	15.4	2.2	17. 1	23.4

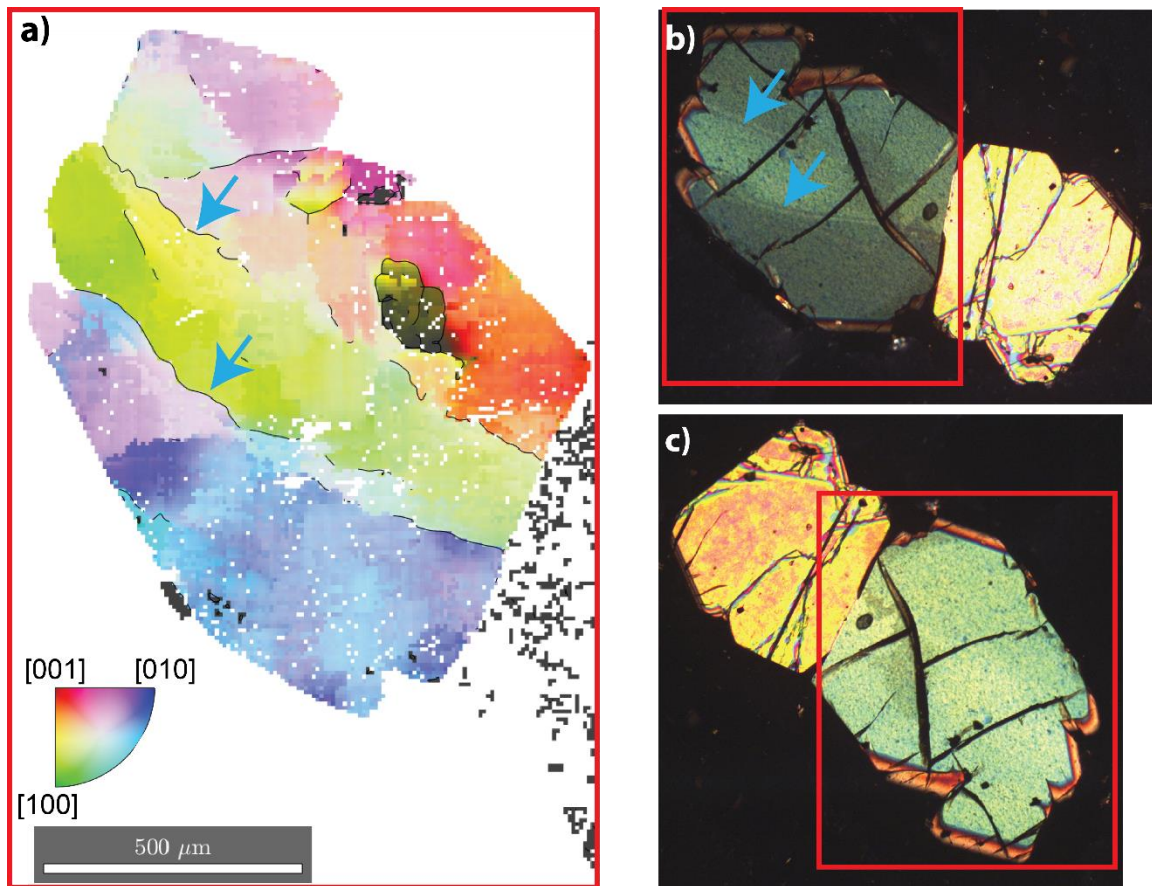
Supplementary Table 6-Details of spectrometers used for WDS EPMA maps.

Element	Spectrometer
Al	LTAP
Ca	PET
P	LPET
Al	TAP
Fe	LIF

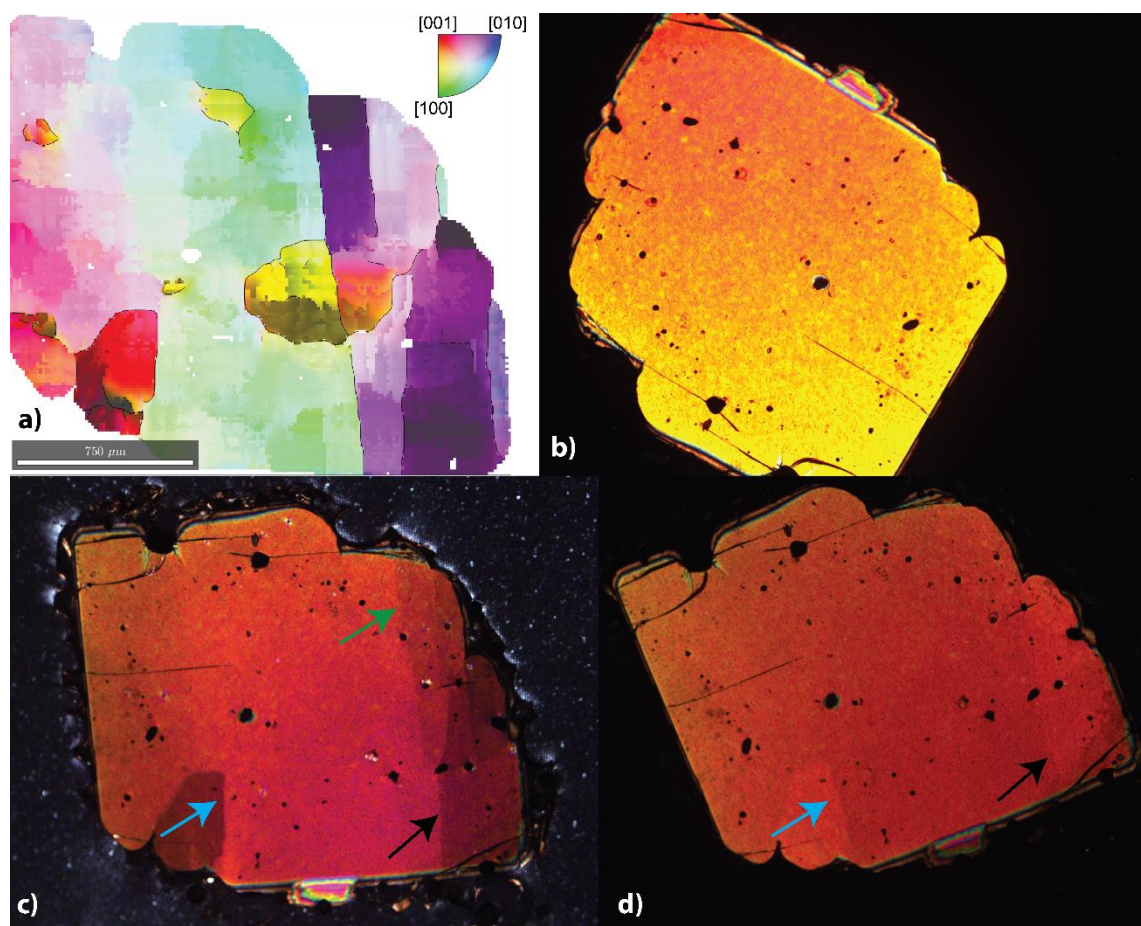
Supplementary Figures



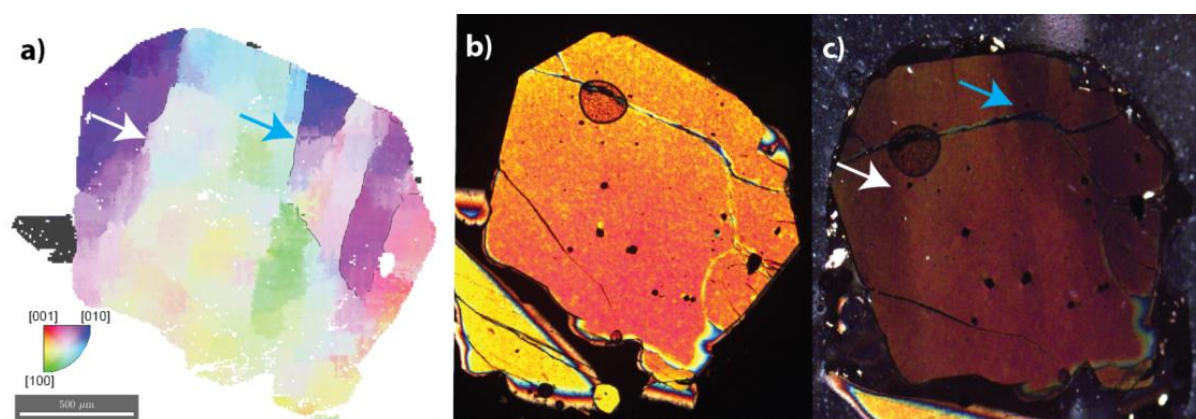
Supplementary Figure 1– Comparison of EBSD-derived IPF map (panel **a**; scaled to 2°) with photos taken using a high-spec optical microscope (panels **b-c**; Zeiss Axioscope A1). Only a small number of the prominent lattice distortions observed in panel **a**) are visible when viewed with an optical microscope (and only within 5° of the extinction position. Additionally, those visible in **c**) when the crystal is close to extinction can only be seen when the brightness is turned all the way up. This shows that unless each grain in a thin section is examined individually (and rotated through 90° while constantly adjusting the brightness and contrast), it is exceptionally easy to miss the presence of intracrystalline distortions. Even when care is taken, only distortions with large misorientations (e.g. purple to yellow colors in **a**) are observed.



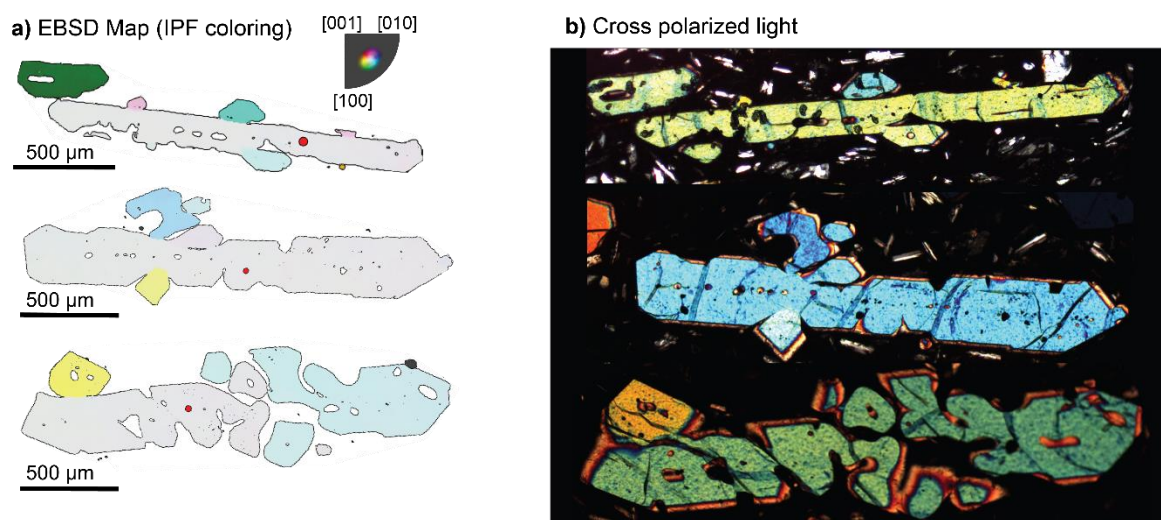
Supplementary Figure 2— Comparison of EBSD-derived IPF map (panel **a**; scaled to 2°) with photos taken using a high-spec optical microscope (panels **b-c**; Zeiss Axioscope A1). The prominent lattice distortions observed in **a**) are almost invisible when viewed with an optical microscope. The two most prominent extinction discontinuities (blue arrows) are only visible when the crystal is within 4° of its extinction position (**b**). In fact, unless the brightness of the microscope is adjusted (as is it in image **b**), it is almost impossible to see these faint color differences.



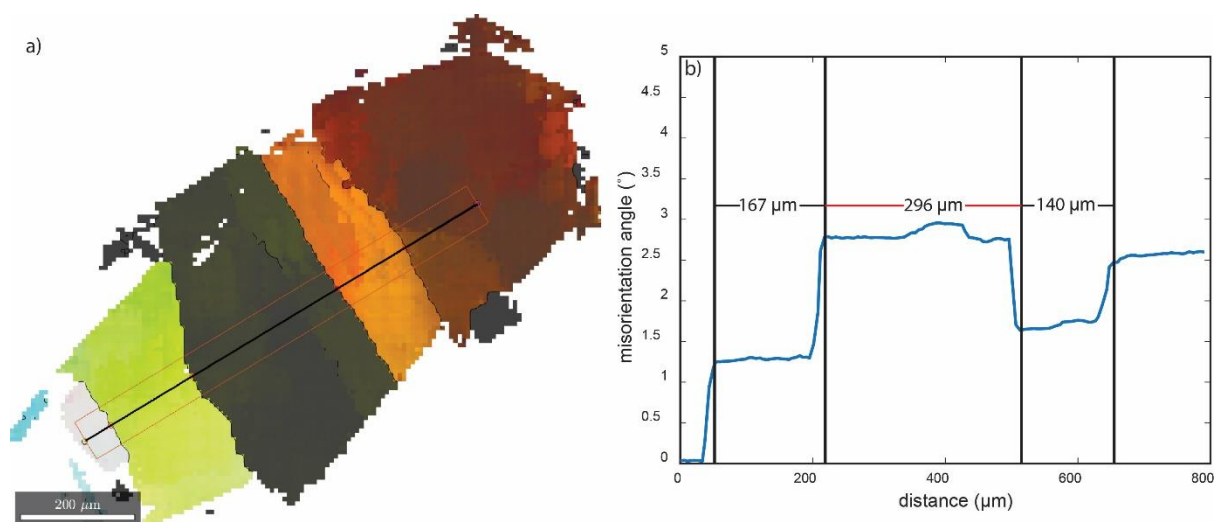
Supplementary Figure 3– Comparison of EBSD-derived IPF map (*panel a*; scaled to 2°) with photos taken using a high-spec optical microscope (*panels b-d*; Zeiss Axioscope A1). The vast majority of low angle boundaries are almost invisible optically (including the prominent transition between green and purple colors in *a*). A few are just visible within 5° of the extinction position (*c*), but only when the brightness of the microscope is turned up.



Supplementary Figure 4– Comparison of EBSD-derived IPF map (*panel a*; scaled to 2°) with photos taken using a high-spec optical microscope (*panels b-c*; Zeiss Axioscope A1). Low angle boundaries are visible within 4° of the extinction position (*c*), but only when the brightness of the microscope is turned up to the max, and the brightness is increased dramatically in the imaging software.



Supplementary Figure 5— Comparison of EBSD-derived IPF map (*panel a*; scaled to 20°) with photos taken using a high-spec optical microscope (*panels b-c*; Zeiss AxioScope A1). Optical photographs of dendritic olivines shown in Fig. 3. The subtle differences in orientation between dendritic branches are difficult to spot (e.g. light blue and white colors in between the left hand and right hand parts of the bottom dendrite).



Supplementary Figure 6— Example linear intercepts for one grain. **a)** The black line on the IPF-colored EBSD map denotes the user selected profile, chosen to be nearly perpendicular to subgrain boundaries. **b)** Misorientations along the profile, averaged laterally over 5 pixels either side of the boundary to remove noise (code adapted from <https://gist.github.com/kilir/410bab7e3e2777200c5e509f1906d225>). The black lines mark the point at which the low angle boundary is crossed at the centre of the profile.